

# Polarimetric analysis of bi-seasonal monostatic and bistatic radar observations of a glacier accumulation zone at Ku-band

Marcel Stefko, *Student Member, IEEE*, Philipp Bernhard, *Student Member, IEEE*,  
Othmar Frey, *Senior Member, IEEE*, and Irena Hajnsek, *Fellow, IEEE*

**Abstract**—We present ground-based Ku-band radar observations of the snow cover on top of the Great Aletsch Glacier carried out over two observation periods, in August 2021 and in March 2022. The observations were carried out with the combined mono/bistatic version of KAPRI, a full-polarimetric radar system, and revealed substantial differences between the scattering behaviour of the snow cover between the two seasons. We analyze the spatial and temporal behaviour of parameters including temporal decorrelation, the scattering entropy, the mean polarimetric alpha angle, and the co- and cross-polarized phase differences. The results indicate that snow cover decorrelates at Ku-band on the timescales of 4-12 hours in winter and summer, which has implications for repeat-pass methods with long temporal baselines. The analysis of the co-polarized phase difference in winter indicates that the parameter is prone to phase wrapping. In summer, its value exhibits smooth spatial trend and a strong sensitivity to changes in incidence angle and liquid water content. The bistatic cross-polarized phase difference also acquires a non-zero value, indicating the presence of non-reciprocal scattering, which has implications for possible calibration procedures of bistatic systems. The presented results aim to serve as a reference for snow scattering behaviour at Ku-band, which can aid planning of future data acquisition campaigns and satellite missions.

**Index Terms**—Bistatic radar, snow remote sensing, polarimetry, interferometry

## I. INTRODUCTION

### A. Snow and ice investigations at Ku-band

The Ku-band frequency range of the electromagnetic spectrum (between 12 GHz and 18 GHz) is attractive for radar investigations of snow and ice [1]–[4]. This is due to the relatively short but non-zero penetration depth into dry snow, which allows a large fraction of the incident radio waves to interact with the snow volume, thus providing opportunities for probing of the physical properties of the snow layer, especially when the layer thickness is insufficient for use of lower frequency bands such as the X-band [5], [6]. The snow parameters of interest include, among others, the snow water

equivalent (SWE) [2], [7], [8], grain size and autocorrelation length [9], [10], snow anisotropy [11], [12], or firn depth [13]. Several spaceborne synthetic aperture radar (SAR) missions using Ku-band for snow and ice research were proposed in the past decade (CoReH2O [14], SCLP [15, Part II]) and also are under current investigation (TSMM [16]).

### B. Bistatic radar investigations of snow

Bistatic radar (i.e., a radar measurement configuration where the transmitter (Tx) and the receiver (Rx) are spatially separated) is a technology which can potentially provide a complementary method of access to snow parameters to the widely used methods based on monostatic radar data (where the spatial separation of the transmitter and the receiver is negligible). It provides an opportunity to expand the observation parameter space, through variation of the bistatic angle  $\beta$ , which is defined as the spatial angle between the transmitter and the receiver from the point of view of the scatterer. Observations under varying values of  $\beta$  provide access, e.g., to a larger number of polarimetric parameters [17], [18]. This bistatic parameter space remains relatively unexplored, mainly due to bistatic radar's higher operational complexity as opposed to monostatic radar. The only bistatic spaceborne mission currently operating is TanDEM-X [19], whose bistatic capabilities were used to characterize snow both through investigations of the bistatic signal phase [20], [21], as well as bistatic intensity variations [22]. However, the nominal operational mode of TanDEM-X involves the use of very small bistatic angles (less than  $1^\circ$ ). There are currently no bistatic spaceborne missions with larger bistatic angles. Ongoing interest in further development of bistatic radar missions is reflected in current proposals of spaceborne radar missions such as Harmony [23], as well as past proposals [24]–[27].

Modeling research of snow and ice has so far focused primarily on integrating passive and monostatic active radar observations [9]–[13], [28]–[31]. However, it should be noted that many radar devices (even those conventionally considered monostatic, such as SnowScat [32]) have a non-zero spatial separation between the transmitting and receiving antenna. In certain cases (especially at short ranges), this separation can result in a bistatic angle value which can non-negligibly affect the observed backscatter, especially in volumetric scattering media such as snow [22, Section 4.3]. Polarimetric investiga-

Marcel Stefko and Philipp Bernhard are with the Chair of Earth Observation and Remote Sensing, Institute of Environmental Engineering, ETH Zurich, 8093 Zurich, Switzerland (e-mail: stefko@ifu.baug.ethz.ch).

Othmar Frey is with the Chair of Earth Observation and Remote Sensing, Institute of Environmental Engineering, ETH Zurich, 8093 Zurich, Switzerland, and also with GAMMA Remote Sensing AG, 3073 Gümligen, Switzerland.

Irena Hajnsek is leading the Chair of Earth Observation and Remote Sensing, Institute of Environmental Engineering, ETH Zurich, 8093 Zurich, Switzerland, and also with the Microwaves and Radar Institute, German Aerospace Center, 82234 Weßling, Germany.

tion of snow properties is also a subject of ongoing research [11], [13], [28], [31], [33]–[41].

### C. Scattering characteristics of snow

Scattering characteristics of snow are strongly dependent on the properties of the incident radiation (frequency, polarization), physical parameters of the snow medium (grain size, water content, layer parameters), as well as observation geometry (incidence, scattering angle). Extensive review literature is available on the topic, e.g., [4], [42]–[45]. In the following paragraphs we shortly summarize the most relevant properties of snow with regard to our radar measurements.

Liquid water content has a strong effect on dielectric properties of snow, and thus strongly affects backscatter intensity, which becomes much weaker as water content increases. Furthermore, the penetration depth becomes much shorter with increasing water content due to absorption. This causes the majority of backscatter from wet snow to come from the uppermost layer of the medium with penetration depth on the order of only a few centimeters at Ku-band [46, Section 4.6], [47], and thus limits the possibilities of probing the deeper layers. Conversely, dry snow allows strong penetration of several meters at Ku-band [46, Figure 4.15], and is a strongly scattering and weakly absorbing medium.

Seasonal snow often exhibits an anisotropic orientation of ice crystals and anisotropy of the large-scale structure, which can impose a polarization-dependent phase delay on the scattering waves. [11] The co-polar phase difference (CPD) [11], [13], [48] defined here as

$$\phi_{\text{HH-VV}} = \phi_{\text{HH}} - \phi_{\text{VV}} = \arg(S_{\text{HH}}S_{\text{VV}}^*) \quad (1)$$

quantifies the difference between the phase of the horizontally-polarized transmitted and received waves  $\phi_{\text{HH}}$  and the vertically-polarized equivalents  $\phi_{\text{VV}}$ . The CPD is often used to characterize this polarization-dependent delay, and is strongly affected by changes in snow metamorphism and depth [11], [13]. Observations at L- to Ku-band have been used to infer structural properties of the snow cover from CPD measurements [11], [13]. The short wavelength of the Ku-band makes the CPD very sensitive to small variations of these properties, however it also makes it potentially prone to phase-wrapping already at layer depths of several tens of centimeters, especially at high incidence angles.

The cross-polarized phase difference (XPD) [49]

$$\phi_{\text{HV-VH}} = \phi_{\text{HV}} - \phi_{\text{VH}} = \arg(S_{\text{HV}}S_{\text{VH}}^*), \quad (2)$$

quantifies the phase difference between the two cross-polarized channels, HV and VH. In the monostatic case, the reciprocity principle dictates that  $S_{\text{HV}} = S_{\text{VH}}$ , and thus the XPD is zero by definition [50]. This fact is often used for calibration of cross-polarized channels [49]. However in the bistatic case, the XPD does not necessarily need to be zero. Due to a low availability of bistatic full-polarimetric systems and datasets [51], the XPD has not been as thoroughly explored and modeled as its co-polarized counterpart. *Note:* Some publications may use the name “cross-polarized phase difference” for a different

parameter, such as  $\phi_{\text{HV}} - \phi_{\text{HH}}$  or similar (e.g. [52], [53]). In this publication we use exclusively the definition in eq. (2).

The two main scattering processes occurring in snow are surface scattering (from the air-snow boundary, snow-ground boundary, or internal layers such as melt-freeze crusts), and volume scattering occurring throughout the snow volume [44]. Dihedral scattering can also occur from one or several of these boundaries. These processes have different polarimetric signatures – the 4-dimensional Pauli scattering vector [17, Sections 3.2,6.5]

$$\mathbf{k}_p = \frac{1}{\sqrt{2}} \begin{bmatrix} S_{\text{HH}} + S_{\text{VV}} \\ S_{\text{HH}} - S_{\text{VV}} \\ S_{\text{HV}} + S_{\text{VH}} \\ j(S_{\text{HV}} - S_{\text{VH}}) \end{bmatrix}, \quad (3)$$

where  $S$  is the Sinclair scattering matrix and  $j$  is the imaginary unit, is often used to distinguish between these processes. Surface scattering exhibits a large magnitude of the first component  $S_{\text{HH}} + S_{\text{VV}}$ , while volume scattering exhibits a comparatively strong third component  $S_{\text{HV}} + S_{\text{VH}}$ . Dihedral scattering can manifest itself in the second ( $S_{\text{HH}} - S_{\text{VV}}$ ) or third component, depending on the orientation of the scattering surfaces. The fourth component  $j(S_{\text{HV}} - S_{\text{VH}})$  is always equal to zero in the monostatic case, however in a bistatic measurement configuration it can have a non-zero value. [17] A graphical visualization of the Pauli scattering vector component magnitudes is often used for a qualitative analysis of scattering processes occurring within the snow medium (e.g. [54]). A quantitative analysis is often performed through second-order polarimetric parameters, such as the Cloude-Pottier scattering entropy  $H$  and polarimetric alpha angle  $\alpha$  [17, Chapter 7], [55, Section 2.3], [56, Chapter 4], or the roll-invariant incoherent target decomposition [57], [58]. Use of these parameters is of interest e.g. for terrain classification in snow-covered or frozen areas [39]–[41], [59], [60].

Snow is a medium that undergoes significant micro-structural changes over time, with varying rates of change depending on snow type, snow cover age, and ambient conditions. [61] These changes significantly affect the scattering behaviour, and can have a strong effect especially on the interferometric coherence  $\gamma$  and its temporal behaviour, which are important for all radar interferometry-based observation methods. The complex interferometric coherence  $\tilde{\gamma}$  is computed from two single-look complex (SLC) radar images  $s_1$ ,  $s_2$  as follows:

$$\tilde{\gamma} = \frac{\sum_W s_1 s_2^*}{\sqrt{\sum_W s_1^2} \sqrt{\sum_W s_2^2}}, \quad (4)$$

where  $W$  is a boxcar moving window. Its final absolute value  $\gamma$  is constrained between 0 (no coherence) and 1 (full coherence). It is affected by several contributing factors, and can be expressed as [19]

$$\gamma = \gamma_{\text{SNR}} \gamma_{\text{Quant}} \gamma_{\text{Amb}} \gamma_{\text{Rg}} \gamma_{\text{Az}} \gamma_{\text{Vol}} \gamma_{\text{Temp}}. \quad (5)$$

These terms respectively describe the reductions in coherence due to SNR, quantization, ambiguities, baseline decorrelation, relative shift of the Doppler spectra, volume decorrelation, and

temporal decorrelation. The relevance of each individual term varies based on sensor type, observation geometry, and the observed medium. The final term,  $\gamma_{\text{Temp}}$  is the temporal decorrelation between the two acquisitions, which in snow can occur due to, e.g., change of liquid water content (i.e., snowmelt or refreezing), or redistribution of the snow particles due to wind or displacement [62]. At Ku-band, scatterer displacement on the scale of 2-3 mm can already cause significant decorrelation [63, eq. (23)]. Furthermore, temporal decorrelation can also be caused by glacier motion – even if the snow cover on top of the glacier remains stable, the motion of the glacier will over time cause the scatterers to move out of their original range cell, which will also cause the scene to decorrelate. This effect is strongly dependent on the observation parameters, namely the range and azimuth sampling resolutions, and the orientation and rate of glacier flow with respect to the sensor. In general, the value of  $\gamma_{\text{Temp}}$  non-linearly reduces with increasing time between acquisitions. Its temporal behaviour can provide an upper bound on the realistic length of acquisition windows for repeat-pass methods such as differential interferometry or SAR tomography, since after a certain time period, the two acquisitions will no longer be sufficiently coherent. Knowledge of the decorrelation time is thus vital, amongst other use cases, for planning and evaluation of viability of airborne and spaceborne data acquisition campaigns. This is especially true at Ku-band, since temporal decorrelation is generally faster at shorter wavelengths [62].

#### D. Terrestrial radar instruments for snow investigations

While this section focuses on ground-based instruments, airborne radar sensors (e.g., [31], [64]–[69]) are a powerful tool for snow monitoring. As opposed to terrestrial sensors, they usually provide superior spatial coverage, and can be easier to deploy in hard-to-access environments. However, they are usually more costly to operate, and offer only limited capabilities for long-term measurements with fine temporal resolution (i.e., maintaining regular sampling intervals over observation windows on the scales of days to months is difficult).

Comprehensive datasets using different radar imaging modalities in the cryospheric environment with very quick revisit times and virtually unlimited time-series durations can be acquired with terrestrial radar sensors. The following is a (non-exhaustive) list of terrestrial radar sensors employed for cryospheric investigations in the past decade:

- The dual-frequency X-/Ku-band UW-Scat instrument analyzed seasonal backscatter trends of snow cover in relation to snow properties [5], [70].
- As part of Phase A studies for the CoReH2O candidate mission, the NoSREx field experiment [3] carried out active and passive microwave measurements of snow. The active measurements spanning from 9.15 GHz to 17.9 GHz were performed with the SnowScat instrument [32].
- As part of the NASA SnowEx project, the SRT3 full-polarimetric radar performed X- and Ku-band observations of snow cover [71] and the observations were used for parameter retrieval [72], [73].
- The SnowScat [47], [74], [75] and WBSCAT [76] scatterometers are used for measuring microwave signatures of snow in support of the ESA SnowLab project [77]. SnowScat covers the frequency range from 9.2 GHz to 17.8 GHz, WBSCAT from 1 GHz to 40 GHz. Both are used, among other purposes, to investigate the relationship between snow parameters and the corresponding detected radar characteristics, and for tomographic profiling.
- The terrestrial Ku-band radar system KAPRI is capable of bistatic full-polarimetric interferometric imaging of areas kilometers in size [78]. It is based on the terrestrial interferometer Gamma GPRI [79]–[82]. Its bistatic capabilities were previously applied to investigate the occurrence of the coherent backscatter opposition effect in seasonal snow [22]. It was also previously used (in the monostatic configuration) to monitor the Alpine glacier Bisgletscher in the context of a geostatistical analysis of the spatial and temporal behaviors of the atmospheric phase screen (APS) in Ku-band [83], [84], as well as polarimetric analysis of natural terrain [85].

#### E. Contributions of this Article

In August 2021 and March 2022, we carried out time series observations of the Jungfraufirn area of the Great Aletsch Glacier in Switzerland with KAPRI, acquiring a fully-polarimetric interferometric time series of both monostatic and simultaneous bistatic observations of the glacier's accumulation zone. In this article, we

- 1) describe the acquisition setup and the acquired data;
- 2) describe the data processing pipeline, including an updated range correction method to correctly geocode data in the complicated bistatic radar geometry, and to compensate for the topographic phase;
- 3) analyze the temporal decorrelation behaviour of snow cover at Ku-band, including development of a simple model to estimate the effect of glacier drift;
- 4) analyze the observed polarimetric characteristics of the snow cover (both monostatic and bistatic), and their spatial and temporal variation;
- 5) discuss the observed Ku-band scattering behaviour and its implications for multistatic monitoring and modeling of snow and ice at Ku-band.

The paper is organized as follows: Section II describes the observation site and ambient conditions during the measurements, the methodology of the multistatic radar acquisition setup, processing and calibration, in-situ data collection, and data analysis. Section III analyzes the resulting data, namely the spatial and temporal behaviour of coherence (including an assessment of influence of glacier drift), scattering entropy, mean alpha angle, and co- and cross-polar phase differences, both in monostatic and bistatic geometries. A discussion of the behaviour of these parameters and the possible underlying causes is given in Section IV. A conclusion is given in Section V.

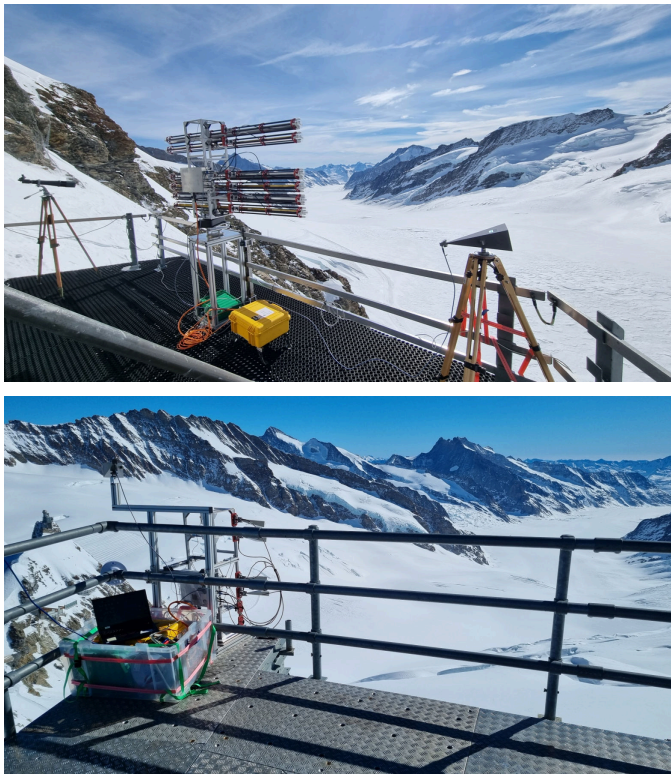


Fig. 1. Photos of both devices deployed at the High Altitude Research Station Jungfrauoch complex. The primary device (top) was deployed on top of the Research Station terrace, the secondary device (bottom) was deployed on the terrace of the East Ridge (*Ostgrat*) building. Both devices observe the Jungfraufirn area, visible in the background of both images. The synchronization antennas pointed along the bistatic baseline are visible in bottom right and top left parts of the two images respectively. The pointing directions of the antennas within the images are approximately south and south-west for the primary and secondary device respectively.

## II. METHODS

### A. Radar observations

An in-depth description of the bistatic KAPRI system used for the observations can be found in [78]. The two devices were deployed on two terraces of the High Altitude Research Station Jungfrauoch, both with direct line-of-sight to the ROIs in the Jungfraufirn area of the Great Aletsch Glacier, and with direct line of sight between each other for synchronization purposes. Photographs of the two devices are shown in Figure 1. A map of the observed area with marked positions of devices and observed scene is shown in Figure 2. Due to the altitude difference between the positions of the two devices forming the bistatic configuration, a special bistatic range shift procedure needed to be developed in order to align the monostatic and bistatic datasets. This procedure is described in detail in this article's supplement, Section S-I. The details of polarimetric calibration of the two devices are described in supplementary Section S-II.

The radars performed repeated acquisitions over the acquired area, with repetition times on the order of 2 – 4 minutes. The winter acquisition spanned  $\sim 30$  hours, while the summer acquisition spanned  $\sim 25$  hours. In summer, for logistical reasons there is a  $\sim 9.5$ -hour interval during the day in which no acquisitions were made. The key parameters of the radar observation periods are summarized in Table I. The

TABLE I  
RADAR ACQUISITION PARAMETERS AND TEMPERATURE CONDITIONS DURING ACQUISITION CAMPAIGNS. THE (D+1) MARK INDICATES THAT THE TIME STAMP CORRESPONDS TO THE DAY FOLLOWING THE START DATE OF THE ACQUISITION PERIOD.

Period	summer	winter
Date (D+0)	2021-08-19	2022-03-02
Time span (UTC)	04:15 – 08:15 17:50 – 05:15 (D+1)	09:00 – 15:40 (D+1)
Angular sweep	1 deg/s	2 deg/s
Repetition time	$\sim 3$ min	$\sim 2$ min
FMCW chirp length	4 ms	
Bandwidth	200 MHz	
Polarization	Full-pol (HH, HV, VH, VV)	
Modality	Monostatic + bistatic	
Temperature (max)	4 °C	-10 °C
Temperature (min)	-2 °C	-15 °C

instruments were operated with similar configuration during both periods, however a faster azimuthal sweep velocity was chosen in winter, in order to ensure smooth operation of the moving parts at low temperatures – this results in shorter integration time in winter and an associated reduction of SNR (of expected magnitude of 3 dB) as compared to the summer configuration.

### B. Area description and in-situ data

The observed area is situated in the area of the Jungfraufirn, one of the three main tributaries of the Great Aletsch Glacier, which is the largest alpine glacier in the European Alps. It exhibits location-dependent typical flow rates of 20–80 cm/day [21], with annual surface velocity averages up to 200 m/year [86]. The observed area spans altitudes between 2800 and 3600 m asl, with the equilibrium line of the glacier (averaged between years 1865–2006) at approx. 3000 m asl [87].

No fresh snowfall events occurred during the summer nor the winter campaign. As shown in Table I, snow melt was occurring during summer due to above-zero temperatures. In winter, temperatures remained well below zero and no snow melt was observed. Weather station data from a nearby automated meteorostation during the observation periods can be found in supplementary Fig. S2.

Several snow pits were dug over the course of the winter campaign, and vertical profiles of snow density, temperature, and grain size were acquired. The location of snow pits is shown in Fig. 2. In summer no snow pits were dug due to logistical reasons. In summer the snow cover showed to be hard, recrystallized and firn-like, caused by repeated melt-freeze events over the course of the preceding season. In winter, snow pits revealed a fresh seasonal snow layer of more than 2 meter depth at each site. Snow pit data showing the vertical profiles of snow grain size, density and temperature acquired over the course of the winter campaign can be found in supplementary Fig. S3. An exemplary photo of the snow pit is shown in supplementary Fig. S4.

### C. Regions of interest

For the time series analysis, several regions of interest (ROIs) were defined, encompassing different parts of the

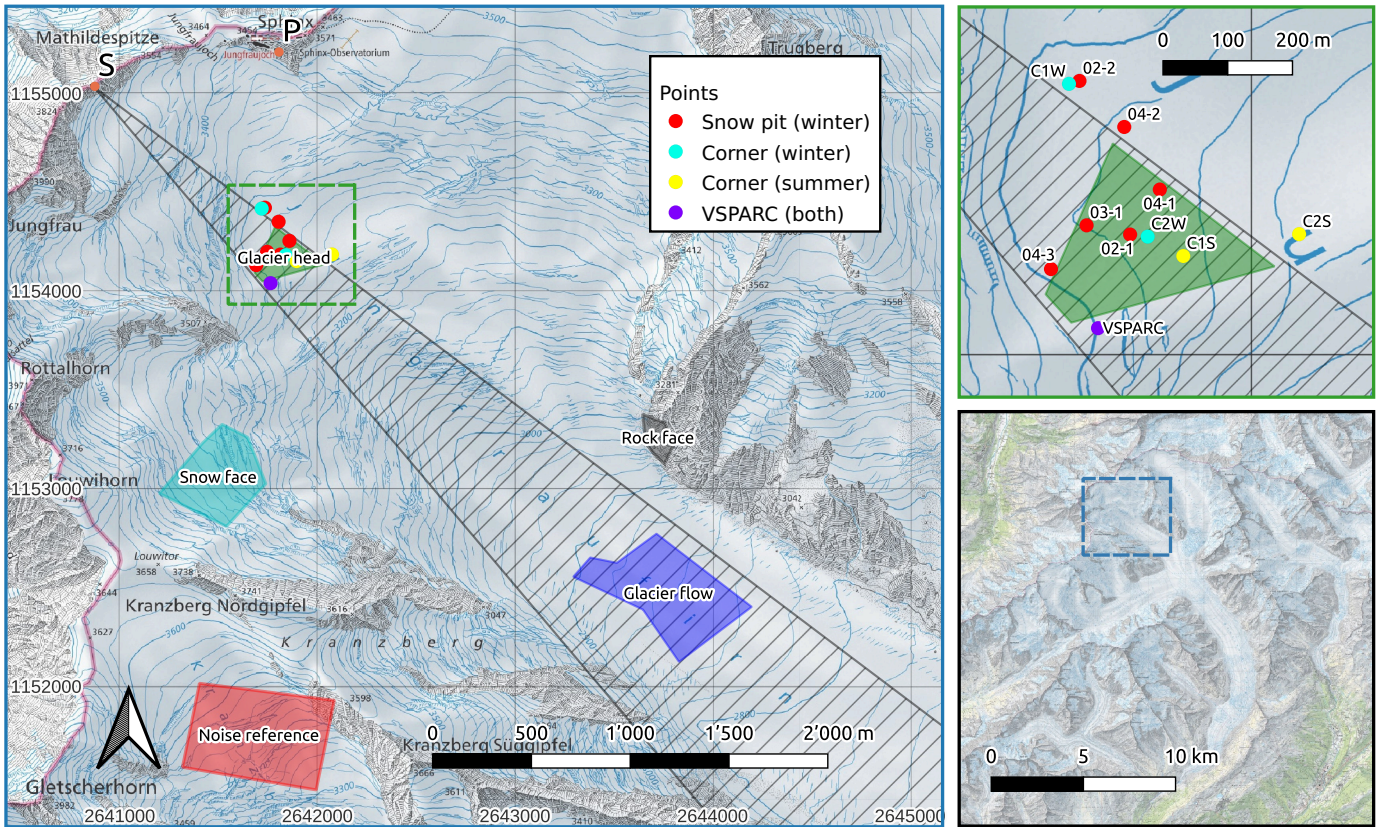


Fig. 2. Map of the observed area of the Jungfrau region of the Great Aletsch Glacier. In the left map, the positions of the primary and secondary radar are marked in the top left of the figure as P and S respectively. The regions of interest (ROIs) are marked as colored polygons. The locations of the six snow pits are marked as red points. C1S, C2S and C1W, C2W mark the positions of the two reference corner reflectors in summer and winter respectively. VSPARC denotes the position of the active radar calibrator. The patterned triangle denotes the coverage of the secondary receiver's antennas (i.e., bistatic coverage). The coordinate grid of the left map corresponds to the CH1903+LV95 coordinate system (EPSG:2056). The two smaller maps on the right side of the figure respectively show a zoomed-in detail of the “Glacier head” ROI area (top), and an overview of the position of the campaign site within the Great Aletsch Glacier region (bottom). Precise extents of the individual sub-region maps can be identified as hashed rectangles with color corresponding to the sub-region map's outline color.

observed scene. The ROIs are shown in Figure 2 and described in Table II. Due to the limited coverage of the bistatic receiver's antennas, bistatic data is only available from two of the ROIs. During certain periods of both summer and winter campaigns, a corner reflector was placed within the “Glacier head” ROI for purposes of polarimetric calibration. To avoid biasing the measurements, the placement locations of the corner reflector were masked out from the dataset before polarimetric/coherence analysis.

TABLE II  
DESCRIPTION OF ROIS.

ROI label	Surface type	Approx. range	Bist. coverage	$\beta$
Glacier head	Snow	800 m	yes	$\sim 40^\circ$
Glacier flow	Snow	3000 m	yes	$\sim 10^\circ$
Rock face	Rock	2500 m	no	N/A
Snow face	Snow	2000 m	no	N/A

#### D. Temporal coherence analysis

In order to explore the behaviour of temporal decorrelation  $\gamma_{Temp}$ , the contribution of all other effects in Eq. (5) needs to be quantified. Several of these terms (described in-depth in

[19]) can be neglected due to the setup of the measurement – zero volume decorrelation can be assumed since there is zero spatial baseline between the individual repeat-pass measurements ( $\gamma_{Vol} \approx 1$ ) [88]. Due to the high bit depth of the receiver's ADC (14 bits/sample), quantization error [89] can also be neglected ( $\gamma_{Quant} \approx 1$ ).

Range and azimuth ambiguities can have a contribution towards biasing of coherence through the term  $\gamma_{Amb}$ . Such ambiguities would also appear coherently in all interferograms, and could thus bias the coherence estimates. The magnitude of their effects on coherence can be approximated by [19, Eq. 26]

$$\gamma_{Amb} = \frac{1}{(1 + RASR)(1 + AASR)} \quad (6)$$

where RASR and AASR are the range and azimuth ambiguity-to-signal ratios, respectively.

Range ambiguities in an FMCW radar could be caused if the pulse repetition interval is too short and echoes from multiple consecutive chirps pass through the band-pass filter simultaneously. To avoid this, the FMCW chirp length  $\tau = 4$  ms was set sufficiently long so that no areas within direct line of sight to the radar system can cause such a phenomenon. Furthermore, topography-caused multi-path effects could cause presence of range ambiguities in particular scenarios, such as when the

ROI is on a face of a hill, and a flat plateau is present between the radar and the ROI [90]. In this experiment, most ROIs do not satisfy this condition and thus no multipath effects are expected. One possible exception could be the ‘‘Snow face’’ ROI, since a flat plateau is present between the primary device and the ROI (approximately around the location of the ‘‘Glacier head’’ ROI). While the ‘‘Snow face’’ ROI has a stronger radar brightness as opposed to the plateau due to a steeper local incidence angle, which should mitigate the effect, a certain degree of influence of multipath scattering on coherence estimates of the ‘‘Snow face’’ ROI can not be definitively excluded. This needs to be kept in mind for coherence analysis of the ‘‘Snow face’’ ROI. The coherence estimates in other ROIs are not affected, and for these ROIs the range ambiguities can be assumed as negligible ( $RASR \approx 0$ ).

The primary device’s antennas have a one-way peak side-lobe ratio (PSLR) of  $-15$  dB. For the primary device, this ratio is applied both ways, resulting in negligible coherence loss:

$$AASR_{\text{mono}} = -30 \text{ dB} \implies \gamma_{\text{Amb,mono}} = \frac{1}{1 + 10^{-3}} > 0.99 \quad (7)$$

In the bistatic case, the return path provides no sidelobe attenuation, thus the estimated decorrelation is

$$AASR_{\text{bist}} = -15 \text{ dB} \implies \gamma_{\text{Amb,bist}} = \frac{1}{1 + 10^{-1.5}} \approx 0.97 \quad (8)$$

this value is also negligible compared to the remaining terms and can thus be neglected ( $\gamma_{\text{Amb}} \approx 1$ ). Azimuth ambiguities stronger than those calculated above (eqs. (7) and (8)) could be present when imaging dark regions situated close to much brighter scatterers (such as corner reflectors), due to the sidelobes of the real-aperture antennas. The area around the corner reflectors placed in the ‘‘Glacier head’’ ROI was masked out from corresponding monostatic data before coherence analysis, in order to avoid biasing the ROI coherence estimates by their scattering response. The ROIs are thus not expected to be affected by especially bright azimuth ambiguities, as there were no comparatively brighter scatterers within their vicinity.

1) *Glacier drift*: Due to the real-aperture nature of the measurement there is zero shift of the Doppler spectra, and due to zero spatial baseline the incidence angle on flat surfaces remains constant. The only factor affecting terms  $\gamma_{Rg}$  and  $\gamma_{Az}$  is thus possible mis-coregistration of datasets. This misregistration can be caused by glacier drift over time, since it can cause scatterers to move out of their original range cell. We can introduce a term

$$\gamma_{\text{Drift}} = \gamma_{Rg} \gamma_{Az} \quad (9)$$

which represents the drop of temporal coherence between times  $T_0$  and  $T$  which occurs when glacier displacement along range and azimuth  $d_{\text{rng}}, d_{\text{azm}}$  accumulates a non-negligible value compared to the resolution cell dimensions  $\delta_{\text{rng}}, \delta_{\text{azm}}$ . The value of  $\gamma_{\text{Drift}}$  starts at 1 when  $T = T_0$ , and reduces to 0 once drift causes all the original scatterers to leave the range

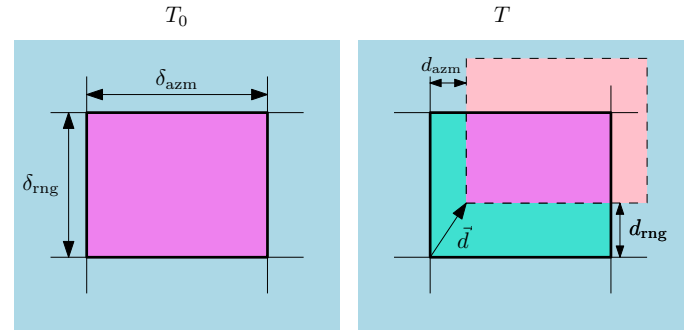


Fig. 3. Linear model visualizing the relationship between glacier drift  $\vec{d} = (d_{\text{rng}}, d_{\text{azm}})$  and the coherence loss  $\gamma_{\text{Drift}}$ . At time  $T_0$ , all original scatterers (violet) are present in the range cell, thus  $\gamma_{\text{Drift}} = 1$ . As the glacier drifts, part of the original scatterers depart the range cell (light pink), while new scatterers enter the range cell (cyan). The drift coherence factor  $\gamma_{\text{Drift}}$  thus reduces according to eqs. (9), (10), and (11).

cell. Figure 3 visualizes this phenomenon. The values of  $\gamma_{Rg}$  and  $\gamma_{Az}$  can be approximated as [19]

$$\gamma_{Rg} \approx \text{sinc}\left(\pi \frac{d_{\text{rng}}}{\delta_{\text{rng}}}\right), \quad (10)$$

and equivalently for the azimuth shift

$$\gamma_{Az} \approx \text{sinc}\left(\pi \frac{d_{\text{azm}}}{\delta_{\text{azm}}}\right). \quad (11)$$

Thus, if it is not possible to correct the drift effect by precise coregistration, its influence can be arbitrarily mitigated by decimation of the SLC (i.e. increasing the resolution cell dimensions through downsampling), which increases  $\delta_{\text{rng}}$  and/or  $\delta_{\text{azm}}$ .

Glacier drift rate can be estimated from KAPRI data using repeat-pass differential interferometry, provided that the temporal sampling rate is dense enough to avoid phase unwrapping errors caused by rapid drift of atmospheric phase screen variations. The drift along the slant-range direction  $d_{\text{slant-range}}$  is related to total horizontal drift  $d_{\text{horiz}}$ :

$$d_{\text{horiz}} = \frac{d_{\text{slant-range}}}{\cos \phi_{\text{drift}} \sin \theta_{\text{inc}}}. \quad (12)$$

In this equation  $\phi_{\text{drift}}$  is the angle between the slant-range look vector and the glacier drift vector, and  $\theta_{\text{inc}}$  is the incidence angle.

KAPRI’s non-decimated range sampling resolution is 0.75 m. Using a range decimation factor of 6, the effective range cell size is increased to  $\delta_{\text{rng}} = 4.5$  m. The azimuthal width of the range cell is range-dependent (due to the real aperture). Using a beamwidth of  $0.35^\circ$  the width within the ROIs (which are placed at ranges above 800 m) is 5 m or more. An azimuthal decimation factor of 2 will thus result in the range cell width  $\delta_{\text{azm}} \geq 10$  m.

In this publication, we are investigating temporal coherence decays on scales of less than 24 hours. Based on our own data (see Section III-A) as well as satellite measurements [21], we estimate the worst-case drift values for both range and azimuth as  $D_{\text{max}} \approx 0.25$  m. We can thus consider the glacier drift effect non-negligible over temporal baselines longer than several hours, if non-decimated data is used ( $\delta_{\text{rng}} = 0.75$  m,  $\delta_{\text{azm}} \geq 5$  m). Using a  $6 \times$  range decimation

factor and a  $2\times$  azimuth decimation factor, the upper ceiling of the effect of glacier drift on temporal coherence after 24 hours can be estimated as a negligible value of

$$\gamma_{\text{Drift},24\text{-hr}} = \text{sinc}\left(\pi \frac{0.25 \text{ m}}{4.5 \text{ m}}\right) \text{sinc}\left(\pi \frac{0.25 \text{ m}}{10 \text{ m}}\right) > 0.99. \quad (13)$$

For comparison, using non-decimated data would result in a 24-hour drift coherence loss of  $\gamma_{\text{Drift},24\text{-hr}} = 0.82$  – this would cause a 20% underestimate of coherence within ROIs located on the glacier, thus potentially overestimating temporal decorrelation rates, which are discussed in the next section.

2) *Temporal decorrelation*: The two remaining terms have the biggest impact on the coherence of the measurement:

$$\gamma \approx \gamma_{\text{SNR}} \gamma_{\text{Temp}}. \quad (14)$$

The SNR term varies greatly depending on range distance, local incidence angle, and scattering properties. Its value can be estimated from the data by dividing the multi-looked intensity (MLI) by the noise floor. Then the decorrelation due to noise can be estimated as [91]

$$\gamma_{\text{SNR}}[T_1, T_2] = \frac{1}{\sqrt{(1 + \text{SNR}_{T_1}^{-1})(1 + \text{SNR}_{T_2}^{-1})}}, \quad (15)$$

where  $\text{SNR}_T$  denotes the signal-to-noise ratio of the acquisition taken at time  $T$ . This ratio can change over time in case of changes in the observed scene (such as snowmelt/refreezing), or changes in the received (e.g. thermal drift). The temporal evolution of the temporal decorrelation starting at time  $T_0$  can thus be estimated from the observed coherence  $\gamma[T_0, T]$  as

$$\gamma_{\text{Temp}}[T_0, T] \approx \frac{\gamma[T_0, T]}{\gamma_{\text{SNR}}[T_0, T]}. \quad (16)$$

Assuming that  $\gamma_{\text{SNR}}$  and  $\gamma_{\text{Temp}}$  are uncorrelated, one can apply the variance formula for error propagation [92] to eq. (14) and derive

$$\Delta\gamma_{\text{Temp}} \approx \frac{\sqrt{\Delta\gamma^2 - \gamma_{\text{Temp}}^2 \Delta\gamma_{\text{SNR}}^2}}{\gamma_{\text{SNR}}}, \quad (17)$$

where  $\Delta\gamma_{\dots}$  signifies the error estimate of  $\gamma_{\dots}$ . This indicates that when SNR is low (and thus  $\gamma_{\text{SNR}}$  is low, such as at high ranges or in the bistatic regime), the uncertainty of the  $\gamma_{\text{Temp}}$  estimate diverges.

### E. Reciprocity principle considerations

Due to the reciprocity principle, in the monostatic case the cross-polarized channels HV and VH should be equal, i.e.  $S_{\text{HV}} = S_{\text{VH}}$ . This fact has been long-used to simplify polarimetric relations by reducing the dimensionality of the data [17], [55], [56], and can also be used for, e.g., calibration [93] or noise filtering [94]. However in the bistatic case the principle no longer generally applies, and in general  $S_{\text{HV}}$  and  $S_{\text{VH}}$  do not need to be equal. It is therefore of interest to investigate the (possibly non-zero) additional polarimetric parameters. These parameters include the cross-polar phase difference  $\phi_{\text{HV-VH}}$ , the cross-polar intensity ratio  $I_{\text{HV}}/I_{\text{VH}}$ , or the fourth (i.e. smallest) eigenvalue  $\lambda_4$  of the coherency matrix  $T$  [17], [94]:

$$T = \left\langle \mathbf{k}_p \cdot \mathbf{k}_p^\dagger \right\rangle. \quad (18)$$

### F. Sign of the phase differences

The sign convention of the polarimetric phase differences is important to define for their proper interpretation and comparison with other literature. In a typical radar processing workflow there are several possible ways the sign of the phase can be flipped (and thus differ between publications), from the choice of coordinate systems (FSA vs. BSA) [17], [56], definition of the phasor rotation direction with increasing range, or ordering of the terms in definitions of phase differences (cf. e.g. [13], [31], [95] which use the HH-VV ordering, and [11], [48], [96], [97] where VV-HH ordering is used).

In this publication, the phase  $\phi$  is defined to decrease with increasing range of the scattering target, i.e. when a target increases its distance from the sensor, the phase of its scattering response decreases:

$$\phi(r) = -\frac{4\pi}{\lambda}r. \quad (19)$$

The implication for polarization phase differences is that if the HH phase center is further away from the radar sensor along range direction as opposed to the VV phase center, and phase wrapping does not occur, the CPD will be negative. For example, if the HH phase center is further away by range distance  $\lambda/8$ , the resulting CPD according to eq. (1) will be  $\phi_{\text{HH-VV}} = \phi_{\text{HH}} - \phi_{\text{VV}} = -\pi/2$ . The same applies for XPD for HV and VH phase centers respectively.

## III. DATA AND RESULTS

To provide a reference frame for interpretation of polarimetric data, in Figure 4 we show the Pauli RGB representation of backscatter images for the morning of both seasons, for both monostatic and bistatic data. Figure 5 shows the time series of estimated SNR (i.e. radar brightness  $\beta_0$  divided by the noise floor) for each ROI defined in Table II. The data shows that the bistatic dataset, especially the ‘‘Glacier flow’’ ROI, exhibits very low SNR once snowmelt sets in in summer. The bistatic SNR in the winter season in this ROI is also low. Care thus has to be taken when interpreting bistatic observations in this region, since noise will have considerable influence.

### A. Glacier drift and temporal coherence

In order to validate the drift estimates described in Section II-D1, we estimated the glacier drift in the ROIs from monostatic KAPRI observations using differential interferometry. Figure 6 shows the slant-range drift rate for both seasons estimated by unwrapping the differential interferometric phase. The slant range drift rate in the glacier ROIs is estimated at approx. 25cm/day. For the ‘‘Glacier flow’’ ROI, this estimate is close to the total drift value, since incidence angle is very shallow and the glacier flow direction is oriented along range. For the ‘‘Glacier head ROI,’’ we can assume that the drift vector has an approximately 45 degree angle  $\phi_{\text{drift}}$  with the range direction. We can thus compute the total drift and the drift components along azimuth and range using eq. (12). Table III shows the calculated displacement values along range and azimuth for the two glacier ROIs.

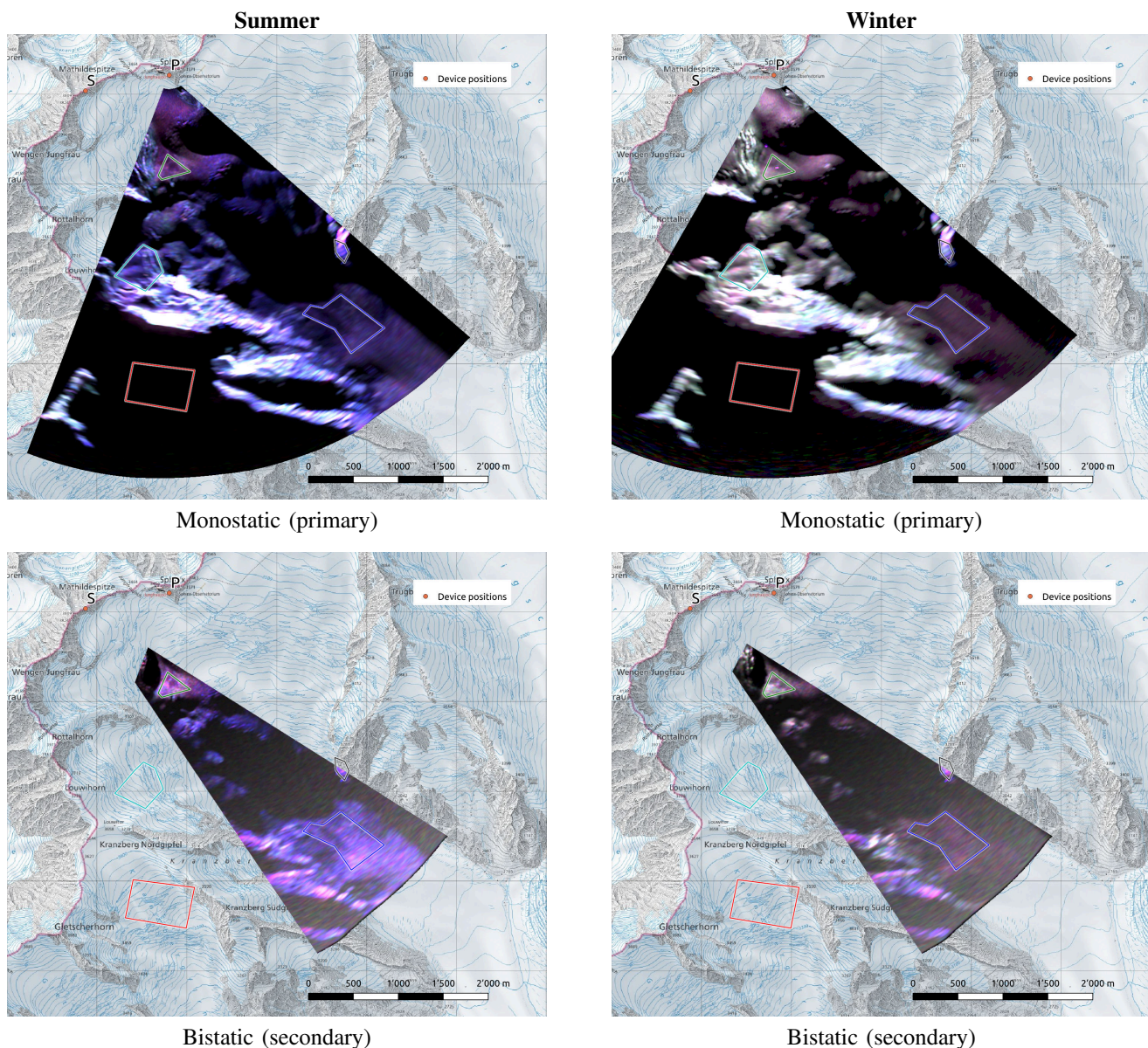


Fig. 4. Comparison of the Pauli representation (B:HH+VV, R:HH-VV, G:HV+VH) of polarimetric data for the summer (left) and winter (right) seasons, showing both monostatic (top) and bistatic (bottom) data. The gamma-scaling of each image was individually adjusted for better contrast and feature visibility. Bistatic images were cropped to show only the area covered by the main lobe of the secondary receiver antennas. The images show that backscatter behavior is dramatically different between the two seasons. The predominantly blue color of summer acquisitions indicates dominance of surface-type scattering, while the mixed color of winter acquisitions indicates a higher diversity of scattering processes. The reduced signal-to-noise ratio of bistatic images due to use of lower-gain antennas is visible as noise in the far-range regions of the images.

TABLE III

DRIFT VALUES OVER A 24-HOUR PERIOD ESTIMATED FROM KAPRI DIFFERENTIAL INTERFEROMETRIC MEASUREMENTS (FIGURE 6). THE DIFFERENCE BETWEEN SUMMER AND WINTER VALUES IS NEGLIGIBLE FOR PURPOSES OF ESTIMATION OF DRIFT EFFECTS ON COHERENCE.

ROI label	$\phi_{\text{drift}}$	$d_{\text{slant range}}$	$d_{\text{horiz}}$	$d_{\text{rng}}$	$d_{\text{azm}}$
Glacier head	45°	23 cm	33 cm	23 cm	23 cm
Glacier flow	0°	21 cm	22 cm	22 cm	0 cm

The drift estimates were then used to assess the influence of range cell drift on temporal coherence estimates and apply decimation in order to mitigate this effect (Section II-D1). Figure 7 shows the resulting time series of estimation of temporal coherence  $\gamma[T_0, T]$  for the two seasons, with the

reference time of day  $T_0$  chosen in the evening of each observation period, in order to avoid further snow melt and maximize time series span. Supplementary Figure S5 shows the maps of this observed coherence  $\gamma[T_0, T]$  over spans of approximately 2, 4, and 8 hours, for the summer and winter seasons respectively.

### B. Second-order polarimetric parameters

For a high-level characterization of scattering processes occurring within the observed areas at Ku-band, and their temporal evolution, we investigate closer the second-order polarimetric parameters, specifically the scattering entropy  $H$  and the mean alpha angle  $\bar{\alpha}$ . The parameters were computed

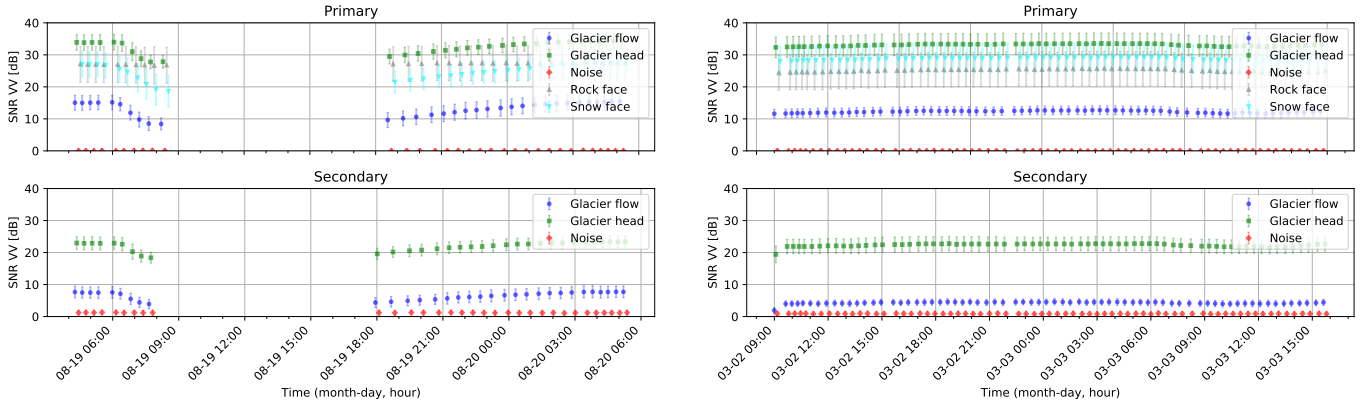


Fig. 5. Time series of signal-to-noise ratio (SNR) in the VV polarization for summer (left) and winter (right) seasons, for both monostatic (top) and bistatic (bottom) data, per ROI. The noise reference level was derived as the mean intensity of all areas with single-pass interferometric coherence  $\gamma < 0.1$ . The bistatic SNR is in general lower than monostatic SNR due to use of lower-gain antennas. In summer, snowmelt during the day causes additional reduction of SNR, leading to critically-low SNR values in the “Glacier flow” ROI of  $< 5$  dB.

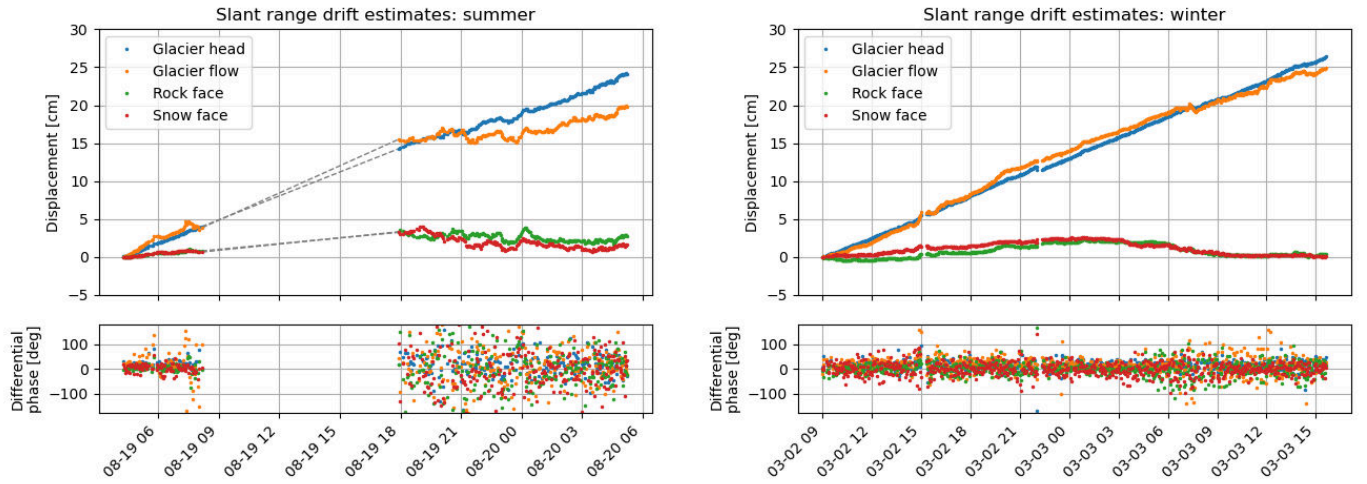


Fig. 6. Slant-range glacier drift of the glacier within individual ROIs estimated from the monostatic radar data by differential interferometry. The drift during the sampling gap in the summer dataset is linearly extrapolated (dashed lines) from the preceding observations. The winter dataset shows stable drift of approx. 21cm/day. In the summer dataset, stronger phase variance is observed. This can be explained by more turbulent atmospheric conditions, lower SNR (see Fig. 5), and a longer sampling rate of approx. 3-4 minutes. This can cause possible phase wrapping, which likely leads to underestimation of the final drift estimate value, especially for the further-placed “Glacier flow” ROI. However, extrapolation of the initial, stable part of the drift curve results in a summer drift estimate of approx. 23cm/day.

from the coherency matrix  $T$  (see eq. (18)) which was computed using a  $5 \times 5$  spatial averaging window.

The scattering entropy  $H$  can serve as a measure of the diversity of scattering processes [17, Chapter 7]. Figure 8 shows the value of entropy in the monostatic dataset for morning and evening of each season. For brevity, maps of these parameters for the bistatic dataset are not shown, however the bistatic behaviour can be assessed through investigation of the time series – this is shown in Fig. 9 and shows monostatic and bistatic values of these parameters for each ROI as specified in Figure 2. This data shows a large difference between the entropy behaviour in summer and in winter. Furthermore, entropy exhibits intra-day variation in summer, while in winter it remains stable throughout the whole observation period, for both monostatic and bistatic datasets.

For an assessment of the type of dominant scattering mechanism [56, Section 4.1.3], [17, Chapter 7], Figures 10 and 11 correspondingly show the maps and time series for the mean alpha angle  $\bar{\alpha}$ . Behaviour similar to scattering entropy  $H$  is

observed, where  $\bar{\alpha}$  has an overall lower value in summer as opposed to winter, and exhibits intra-day variation in summer, while remaining stable in winter.

In order to investigate possible occurrence of non-reciprocal scattering processes (i.e. processes where  $S_{HV} \neq S_{VH}$ ) [17], [55], [94], Figure 12 shows the time series of the relative values of the fourth eigenvalue of the coherency matrix  $\lambda_4$  compared to the sum of all four eigenvalues, i.e. the plotted value is:

$$\hat{\lambda}_4 = \frac{\lambda_4}{\sum_{n=1}^4 \lambda_n}. \quad (20)$$

The data shows a low value of the  $\hat{\lambda}_4$  in the monostatic datasets irrespective of the season. Bistatic datasets however show a higher value, thus indicating possible presence of non-reciprocal scattering.

### C. Polarimetric phase differences

Polarimetric phase differences  $\phi_{HH-VV}$  and  $\phi_{HV-VH}$  can be used for investigation of anisotropy of the snow pack [11], as

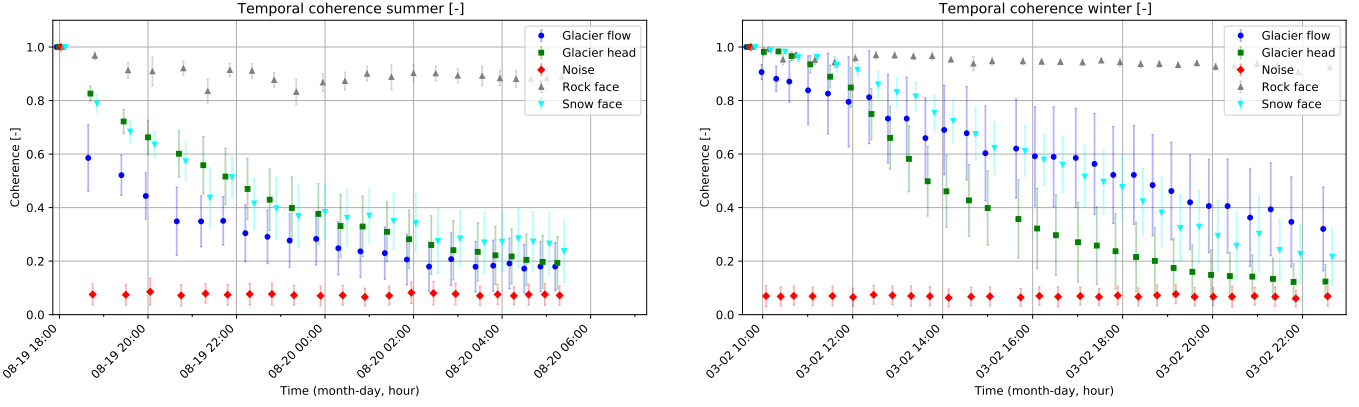


Fig. 7. Time series of coherence  $\gamma[T_0, T]$  for the summer (left) and winter (right) seasons. Time  $T_0$  in summer was chosen in the evening to avoid the increase of liquid water content during the day, and to maximize the uninterrupted time series length. Due to stability of the scene in winter, the choice of  $T_0$  has negligible impact on data in winter. For both seasons, the time axis spans 13 hours. The points and error bars represent the mean and the standard deviation of the coherence within each ROI.

well as investigation of possible non-reciprocal scattering in the bistatic regime [55]. All phase differences shown in this section follow the sign convention described in Section II-F.

In order to assess the spatial and temporal behaviour of the co-polar phase difference  $\phi_{HH-VV}$ , Figures 13 and 14 show the maps of  $\phi_{HH-VV}$  for both devices and seasons, for the morning and evening time respectively. The time series of  $\phi_{HH-VV}$  can be found in supplementary Fig. S6. Similarly to entropy and mean alpha angle, a large difference in behaviour between seasons, and intra-day variation in summer is observed.

The cross-polarized phase difference  $\phi_{HV-VH}$  should have a zero value in the monostatic observations due to the reciprocity principle [50] (this is confirmed in supplementary Fig. S7), and thus the bistatic behaviour is of larger interest, as its non-zero value is an indicator of non-reciprocal scattering. Figure 15 shows the maps of  $\phi_{HV-VH}$  for the secondary device in both seasons, for both the morning and evening time. The time series is shown in supplementary Fig. S8. The data confirms that  $\phi_{HV-VH}$  acquires a non-zero value in the bistatic regime, and the spatial and temporal behaviour varies dramatically between the summer and the winter season.

#### IV. DISCUSSION

##### A. Polarimetric calibration and limitations of the dataset

Polarimetric calibration in the large-angle bistatic regime, where neither the reciprocity principle nor corner reflectors can be used, is usually more challenging than monostatic calibration [78]. The bistatic calibration in this experiment was performed with the VSPARC active calibrator [78], while the monostatic calibration was carried out using a combination of corner reflectors and the application of the reciprocity principle [93]. Table S-I shows the residuals of the polarimetric calibration of the primary device, however these residuals are not available for the secondary device, since a second, independent validation target was not available. The observed data (e.g. bistatic alpha angle  $\bar{\alpha}$ ) and a visual assessment of the Pauli basis scattering in Fig. 4 do suggest correctness of calibration, however this limited validation has to be kept in mind when interpreting bistatic data.

Due to the processing complexity of polarimetric KAPRI data and topographic phase correction, care has to be taken that the shown polarimetric phase difference values in Figs. 13 through 15 are not just an artifact of inaccurate phase compensation. There are several indications that the observed phase differences are real. Firstly, the shown XPD/CPD is relatively constant and no fringes – which are typically present when the topographic phase is incorrectly compensated – are observed. Secondly, the CPD observed in summer behaves similarly between the monostatic and bistatic dataset, starting with a strong offset in the morning and flattening in the evening. Finally, for the XPD, the VSPARC calibrator was placed near the “Glacier head” ROI in the summer acquisitions. It was set to the constant phase response configuration (described by [78, eq. (39e)]), and thus there was zero phase delay between VSPARC’s signal in all polarimetric channels. Accordingly, in the bottom left map in Fig. 15 VSPARC can be seen as a point target exhibiting a zero XPD. There is thus a high degree of confidence that the XPD data in VSPARC’s vicinity is correctly unwrapped and compensated. However, independent validation (preferably with a second cross-polarizing bistatic target placed in a second location) is desirable for future acquisitions to achieve certainty about the observed phase differences.

The combined monostatic/bistatic setup allows us to investigate the behaviour of observed polarimetric parameters as the bistatic angle changes from zero to a relatively high value of  $50^\circ$ . However, the geometry limitations do not allow sampling of a continuous  $\beta$  spectrum up to this maximal value. The sampling is instead limited only to the two ROIs within the bistatic beam (“Glacier head” and “Glacier flow”), with bistatic angle values of  $40^\circ$  and  $10^\circ$  respectively. Bistatic angles other than these values remain unavailable, and thus the behaviour cannot be easily generalized. Furthermore, the ground-based acquisition geometry also results in relatively shallow incidence angles of  $75^\circ$  and  $80^\circ$  in the two ROIs. The snow and rock face ROIs provide a relatively steep local incidence angle due to the mountainous geometry, however are for the same reason more susceptible to foreshortening effects.

In this paper the entropy  $H$  and mean alpha angle  $\alpha$  of the

## Entropy

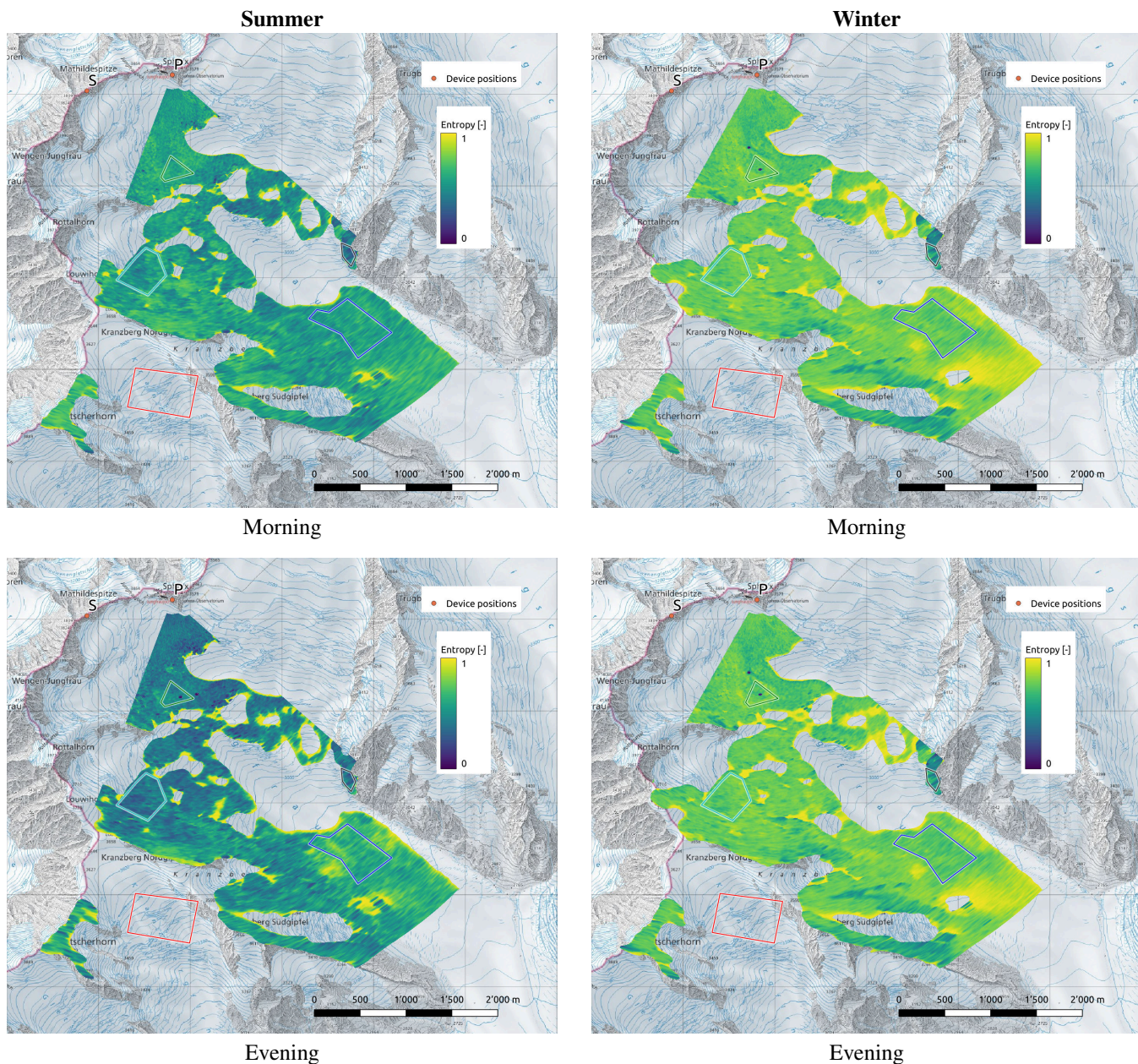


Fig. 8. Comparison of the observed monostatic entropy  $H$  for the summer (left) and winter (right) seasons, for morning (top) and evening (bottom) times of day. In winter, the entropy retains a high value throughout the day. In summer, entropy is comparably lower. It also further reduces during the day and reaches its minimal value after sunset. The exception are exposed rock areas which retain a low entropy value throughout.

Cloude-Pottier incoherent target decomposition [17], [56] are analyzed in detail. Other parameters from decompositions such as the roll-invariant incoherent target decomposition [57] (and, in the case of bistatic observations, its bistatic extension [58]) could potentially provide further detailed insights. However, due to limited spatial extent of the dataset and thus the inability to acquire sufficiently diverse and extensive statistics of different terrain types (especially after the necessary multilooking), such analysis is not carried out here.

### B. Glacier drift and temporal coherence

The estimated glacier drift shown in Fig. 6 and Table III is aligned with the results from a previous investigation using

TanDEM-X data [21, Fig. 15], which determined the median horizontal glacier velocity of  $\sim 0.3$  m/day in the “Glacier head” ROI, and  $\sim 0.2$  m/day in the “Glacier flow” ROI. However, the ROIs lay within regions with low probability of velocity tracking success [21, Fig. 18], and thus have to be interpreted with caution. For comparison, the global ice velocity dataset [98] yields mean velocity values of 0.17 m/day for “Glacier head” ROI and 0.24 m/day for “Glacier flow” ROI, thus showing an opposite trend. This discrepancy (between our observations and the dataset in [98]) could have various causes, for example the 3-year gap between measurements, the difference in the temporal scale of the observations (days vs. years), simplified geometric assumptions in Table III,

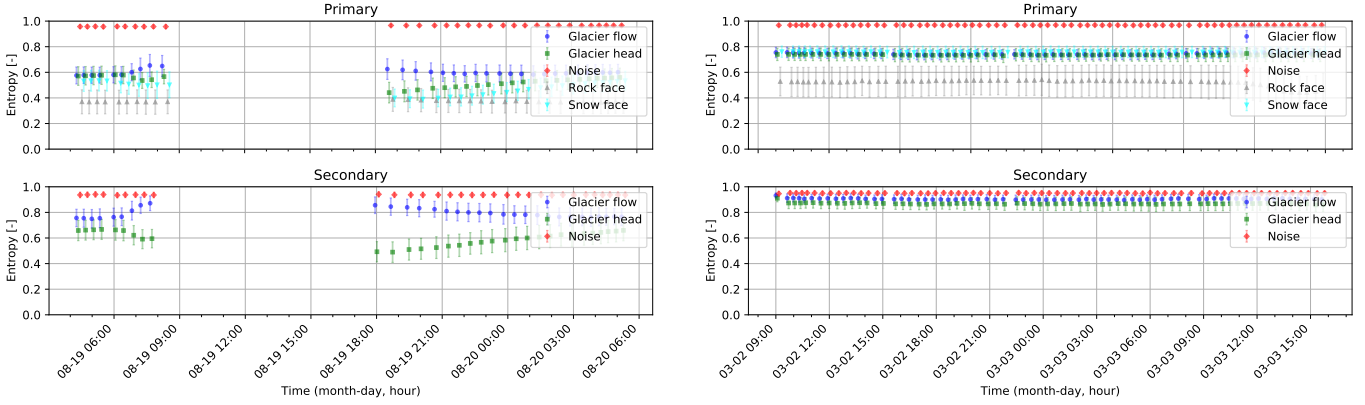


Fig. 9. Time series of entropy  $H$  for summer (left) and winter (right) seasons, for both monostatic (top) and bistatic (bottom) data, per ROI.

uncompensated atmospheric phase screens, etc. However, the objective of the analysis of glacier drift in Section III-A is only to assess its magnitude for purpose of temporal decorrelation analysis as described in Section II-D1 – for this a rough estimate of the drift value is sufficient. The values shown in Table III justify the decimation-based approach of Section II-D1, which mitigates the influence of drift on the observed coherence. We note that due to the temporal constraints of the dataset (measurements done only in 4 days of the year) and limited spatial coverage of the ROIs, the drift data shown in Table III can not be used to draw conclusions about the total mass balance of the glacier.

The temporal decay of coherence shown in Fig. 7 indicates that coherence exhibits an exponential-like decay on the scale of hours during both seasons. In winter the major contributing factor is likely small microstructural variations which, even when small, have a considerable effect at short wavelengths, as temporal decorrelation occurs faster at short wavelength [63]. In summer, the “aged” snowpack can be possibly considered more stable in terms of microstructure, however the considerable and periodic changes in liquid water content can contribute to rapid changes in scattering characteristics and thus cause decorrelation [99]. Since the start time  $T_0$  was chosen in the evening, the snowpack was refreezing during the coherence monitoring window, and thus there was no further loss of coherence due to reduction of SNR. However, the relatively low value of SNR can be a partial contributor to the low coherence estimate, especially in summer in the “Glacier flow” ROI, for which eq. 15 and SNR values from Fig. 5 predict an SNR coherence loss factor  $\gamma_{\text{SNR}} \approx 0.9$ .

The characteristic decorrelation timescale (i.e. the timescale on which coherence reduces to  $1/e \approx 0.36$ ) can be estimated as 4 – 8 hours in summer, and 6 – 12 hours in winter. This has strong implications for repeat-pass interferometric methods – applying repeat-pass interferometric methods with temporal baselines longer than a few hours may not be feasible due to almost complete decorrelation of the snowpack. Spaceborne SAR missions are particularly affected, since their revisit times usually have a value on scale of several days. Spaceborne Ku-band SAR missions might thus not be able to apply repeat-pass interferometric methods over snow-covered areas, unless steps are taken to reduce this temporal baseline, through use of e.g.

constellations.

It should be noted that in some experiments under different conditions and in different observation areas, the decorrelation time of snow cover at Ku-band was observed to be longer – for example, data in [74] shows sustained coherence between Ku-band tomograms of snow cover over baselines up to 14 hours.

The coherence decay observed in [62] at similar wavelengths (16.8 GHz) shows a similar trend to our observations during snow melt, i.e. rapid decay of coherence on the order of hours. However, during the presence of dry snow, in [62] a much lower typical rate of coherence decay was observed, with the snowpack remaining partially coherent ( $\gamma \approx 0.5$ ) for several tens of days. A possible explanation for this discrepancy may be the difference in observation sites and meteorological conditions – our observations were carried out on a high-altitude glacier, with strong wind gusts up to 45km/h (see supplementary Fig. S2). Indeed, in [62], similarly rapid coherence decay was observed during a period of similarly strong wind which followed after fresh snowfall. Furthermore, the snow depths in our study (2-4 m in winter) are much deeper than in [62] where snow depth ranged typically between 20 cm and 80 cm. It could thus be expected that ground signal contributes more considerably to the backscatter in [62] and keeps the coherence high, while the snow volume contributes more in our study, and thus exhibits a higher decorrelation rate due to snow redistribution.

Nevertheless, comparison with the previous studies [62], [74] indicates that our observed rates of decorrelation can not be simply extrapolated to all snow-covered environments, and possibly also not to all times of year in the same environment. Further study is thus needed in order to determine whether the observed rates of decorrelation are also representative for other meteorological conditions and environments.

### C. Second-order polarimetric parameters

1) Entropy: The time series of entropy (Fig. 9) follows an expected trend in all datasets – the polarimetric entropy is high in winter and constant over time, which suggests a large diversity of scattering processes. In summer, the entropy is lower overall, and also exhibits a variation over the course of

## Alpha angle

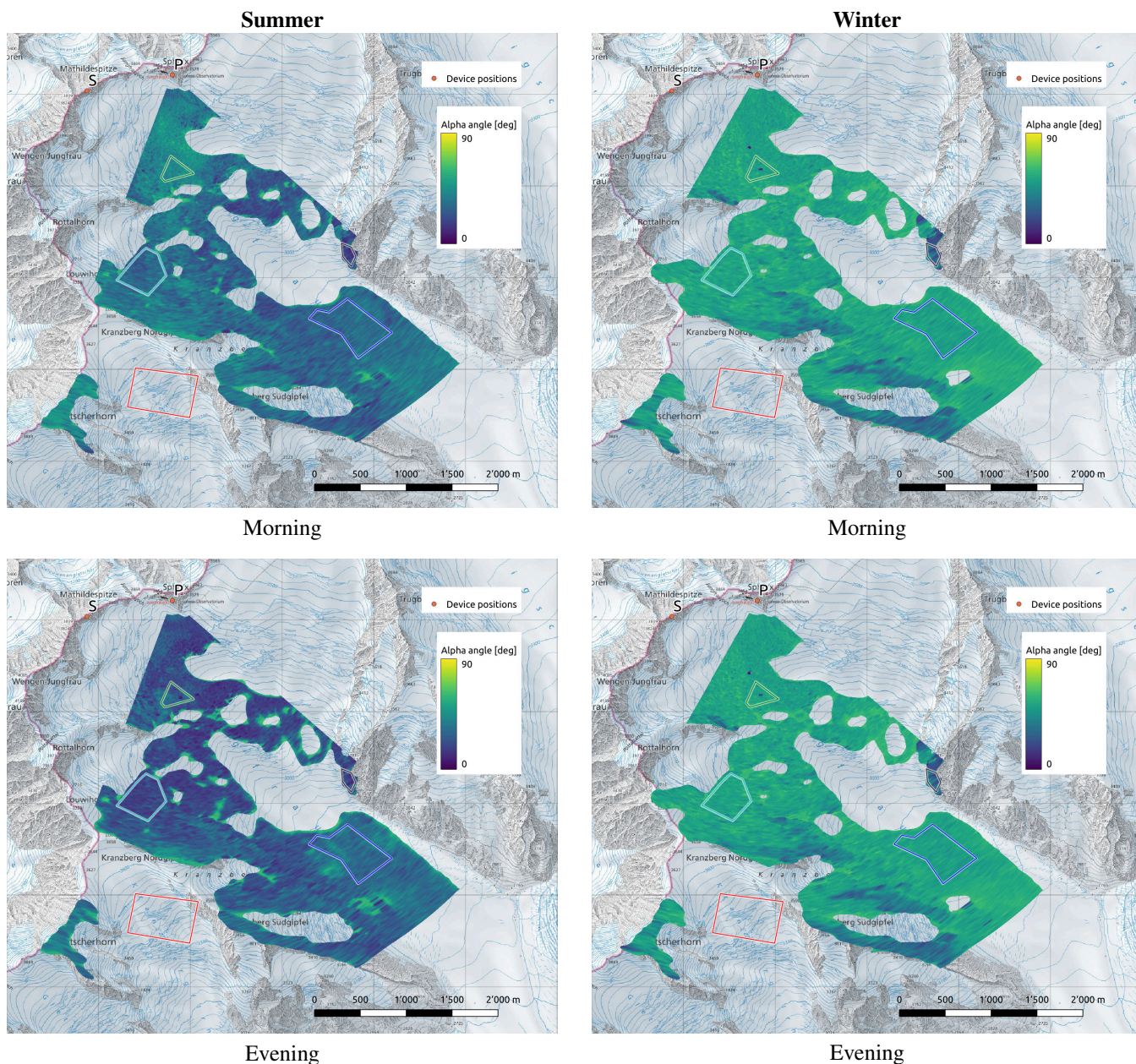


Fig. 10. Comparison of the observed monostatic mean alpha angle  $\bar{\alpha}$  for the summer (left) and winter (right) seasons, for morning (top) and evening (bottom) times of day. In winter,  $\bar{\alpha}$  retains a medium value throughout the day. In summer,  $\bar{\alpha}$  is comparably lower. It also further reduces during the day and reaches its minimal value after sunset, in a manner similar to entropy in Fig. 8. The exception are exposed rock areas which retain a low entropy value throughout.

the day. This suggests that deterministic scattering processes, such as surface scattering, have a higher proportion, which is in agreement with the interpretation that melt-freeze crusts are present close to the surface in summer and cause a contribution of low-entropy surface scattering [17]. Furthermore, the temporal variation indicates that entropy reduces further as snow melt sets in during daytime, which increases liquid water content and reduces penetration depth [46], resulting in even larger contribution of surface scattering to total observed backscatter. The only exception is the behaviour of “Glacier flow” ROI in the bistatic dataset in summer, where the rise in entropy with increasing snow melt can be explained as loss of signal, i.e. the entropy is calculated mostly on noise, which

has very high intrinsic entropy.

2) *Mean alpha angle*: The mean alpha angle  $\bar{\alpha}$  (Fig. 11 exhibits behaviour very similar to entropy, and can be explained with the same interpretation. The value of  $\bar{\alpha}$  between  $40^\circ$  and  $60^\circ$  is in agreement with dominance of volume scattering in winter. Lower values in summer suggest a larger (relative) contribution of surface scattering, and the temporal behaviour is in agreement with increasing contribution of surface scattering due to increased liquid water content, with the “Glacier flow” ROI in the secondary dataset once again exhibiting an exceptional increase due to loss of SNR.

3) *Fourth eigenvalue  $\lambda_4$* : The fourth eigenvalue  $\lambda_4$  of the coherency matrix  $T$  should have a zero value in the monostatic

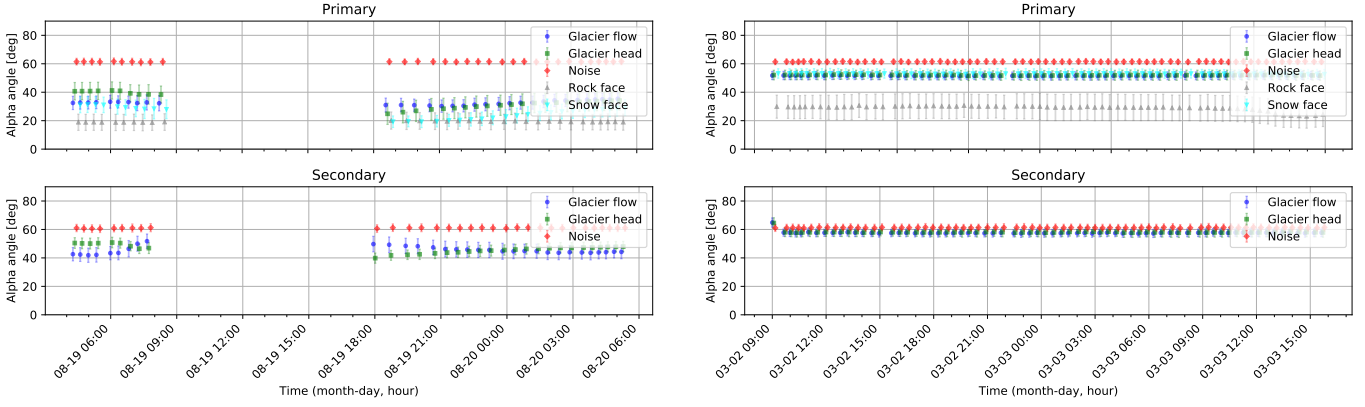


Fig. 11. Time series of mean alpha angle  $\bar{\alpha}$  for summer (left) and winter (right) seasons, for both monostatic (top) and bistatic (bottom) data, per ROI.

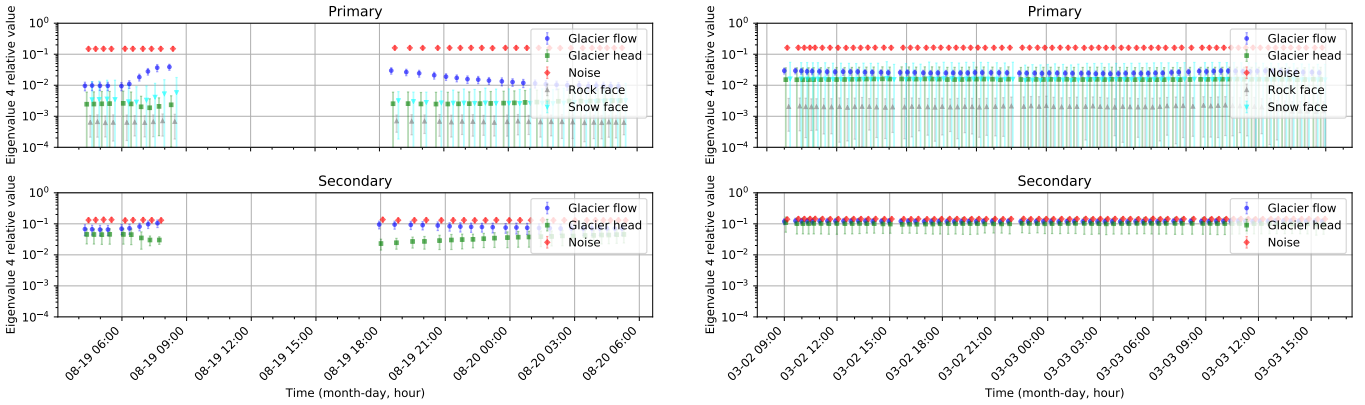


Fig. 12. Time series of the fourth eigenvalue  $\hat{\lambda}_4$  as defined in eq. (20) for summer (left) and winter (right) seasons, for both monostatic (top) and bistatic (bottom) data, per ROI. The y-axis is logarithmic. The primary (monostatic) datasets exhibit an overall low value irrespective of season or time of day. The temporal rise of  $\hat{\lambda}_4$  value in the “Glacier flow” ROI in summer is correlated with the SNR reduction (see Fig. 5). The bistatic datasets (secondary) show a higher value of  $\hat{\lambda}_4$ , indicating presence of non-reciprocal scattering.

case due to the reciprocity principle [94]. This is confirmed in Fig. 12 which shows that the estimate of the value of  $\hat{\lambda}_4$  does not exceed 0.03, with the exception of the evening of the summer period, where noise becomes a considerable factor. The slightly higher estimates in winter can be caused by a higher diversity of cross-polarizing scattering processes which could “leak” into the fourth Pauli component and thus into the fourth eigenvalue. The effect in the monostatic dataset is however very limited and the absolute value remains low.

In the bistatic case,  $\hat{\lambda}_4$  is higher overall – this can be due to several contributing factors. Firstly, the SNR is overall lower in the bistatic case, which could cause an increase in the estimate of  $\hat{\lambda}_4$ . However, the comparison of monostatic summer SNR in “Glacier flow” ROI with the bistatic SNR in “Glacier head” ROI indicates that the bistatic data should have sufficient SNR. The second contributing factor could be a higher diversity of cross-polarizing scattering processes, just like in the monostatic winter data. This however does not completely explain why the value is also high in summer, where cross-polarizing contributions are quite low. The third possible factor is miscalibration, which could cause a contribution in case the amplitudes or phases of cross-polarized channels are not precisely calibrated. This effect certainly can not be excluded, due to factors mentioned in Section IV-A. However,

miscalibration likely is not the only factor, since the higher values of  $\hat{\lambda}_4$  are detected in both seasons which were calibrated separately, and  $\hat{\lambda}_4$  also exhibits a slight temporal trend in the “Glacier head” ROI, which indicates that it is caused by a true scattering signal. Furthermore, the XPD maps shown in Fig. 15 (and timeseries in supplementary Fig. S8) indicate that there are non-reciprocal scattering processes occurring in the scene, which will then result in non-zero value of the fourth Pauli component  $k_{P4} = \frac{j}{\sqrt{2}}(S_{HV} - S_{VH})$ , and non-zero fourth eigenvalue of the  $T$  matrix. The non-zero value of  $\hat{\lambda}_4$  is thus most likely caused by the same non-reciprocal processes that cause the non-zero cross-polarized phase difference, and the quantification of  $\hat{\lambda}_4$  in Fig. 12 can be used as an estimate of the contribution of these processes to total backscatter.

#### D. Polarimetric phase differences

1) *Co-polar phase difference*: The co-polar phase difference  $\phi_{HH-VV}$  (Figs. 13 and 14) exhibits a similar behavior between monostatic and bistatic datasets. In summer, it exhibits an incidence angle dependence which varies with time of day. When the snow cover is frozen (i.e. in the morning),  $\phi_{HH-VV}$  has a strong negative value at low incidence angles (near-range), and trends towards a slight positive value at high incidence angles (far-range), for both the monostatic

Morning acquisitions,  $\phi_{HH-VV}$

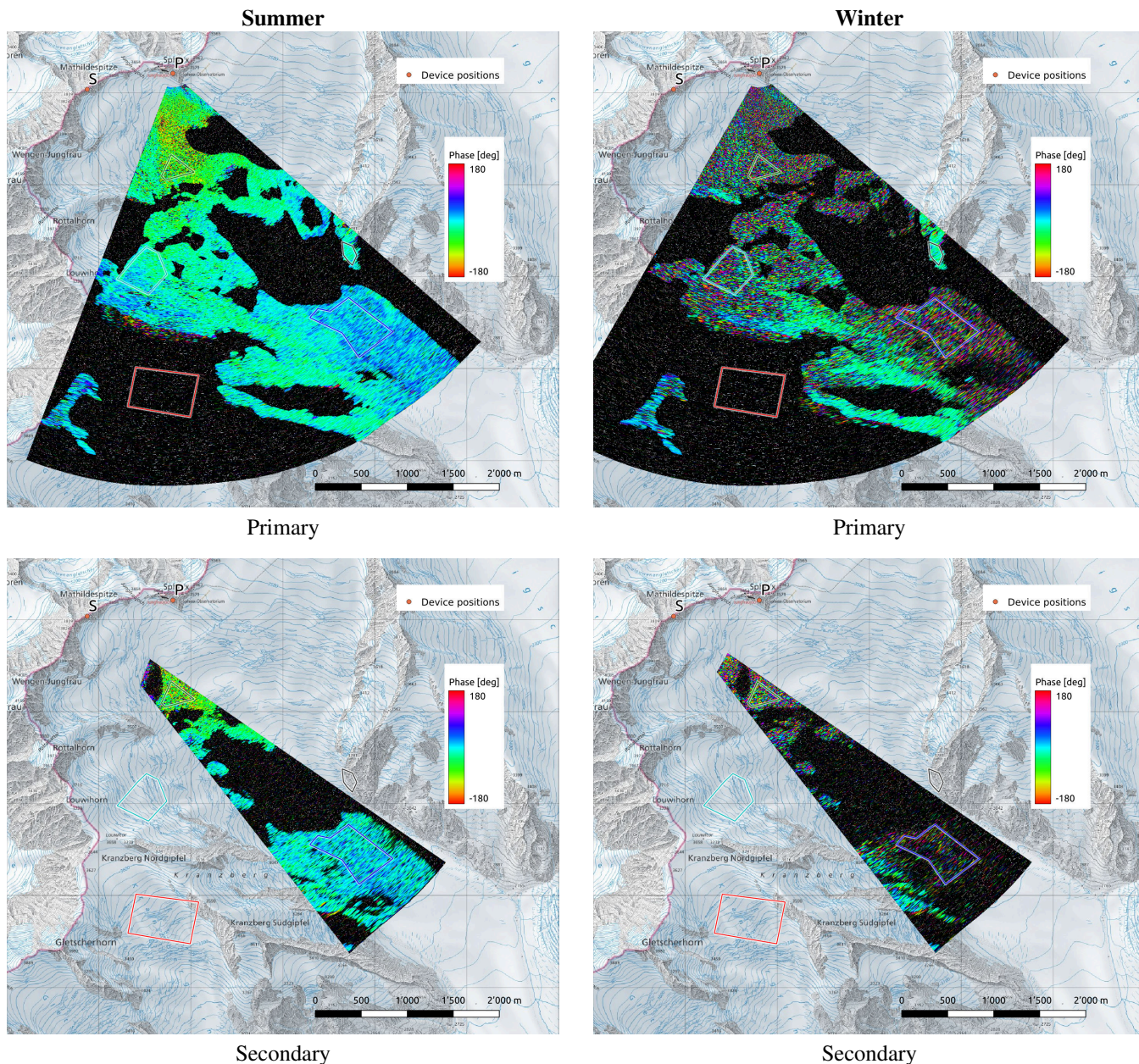


Fig. 13. Comparison of the observed CPD for the summer (left) and winter (right) seasons, for the primary (top, monostatic) and the secondary (bottom, bistatic) dataset. The data was acquired in the morning. In order to enhance the signal, 10 consecutive interferograms were coherently averaged. In summer, the CPD has a “well-behaved” value, and does not appear to exhibit phase wrapping, neither in the monostatic nor the bistatic dataset. It exhibits an incidence angle dependent behaviour, where its value increases with increasing incidence angle. In winter, the CPD considerably varies over very short spatial scales, and appears to exhibit phase wrapping. The exception are exposed rock areas which retain a CPD value of close to 0.

and the bistatic dataset. It is difficult to interpret the change of the sign of CPD between these two areas as an effect caused purely by birefringence, since it would require a large change in the snow cover’s structure and anisotropy between the two observed regions. An alternative interpretation of the change of the sign of CPD could be a change in the relative contribution of dihedral (double-bounce) scattering between the two geometries, where the contribution is larger at lower local incidence angles (i.e. near range). Fig. 4, acquired in the morning, shows a more dominant red color in the near-range region in summer, indicating a higher contribution of dihedral

scattering. Dihedral scattering contribution has opposing effects on phases of the HH and VV channels (increasing the phase of one and decreasing the phase of the other, all else being equal) [17], and thus could cause a sign flip of  $\phi_{HH-VV}$  if the relative contribution of double-bounce scattering to total backscatter changes.

This observed spatial trend of  $\phi_{HH-VV}$  in summer can be compared with literature. The incidence angle dependence has the opposite trend to values observed at X-band in Greenland [31, Figures 3-5] and L-band in Svalbard [100, Figures 8-9], where the  $\phi_{HH-VV}$  phase difference showed divergence from

Evening acquisitions,  $\phi_{HH-VV}$

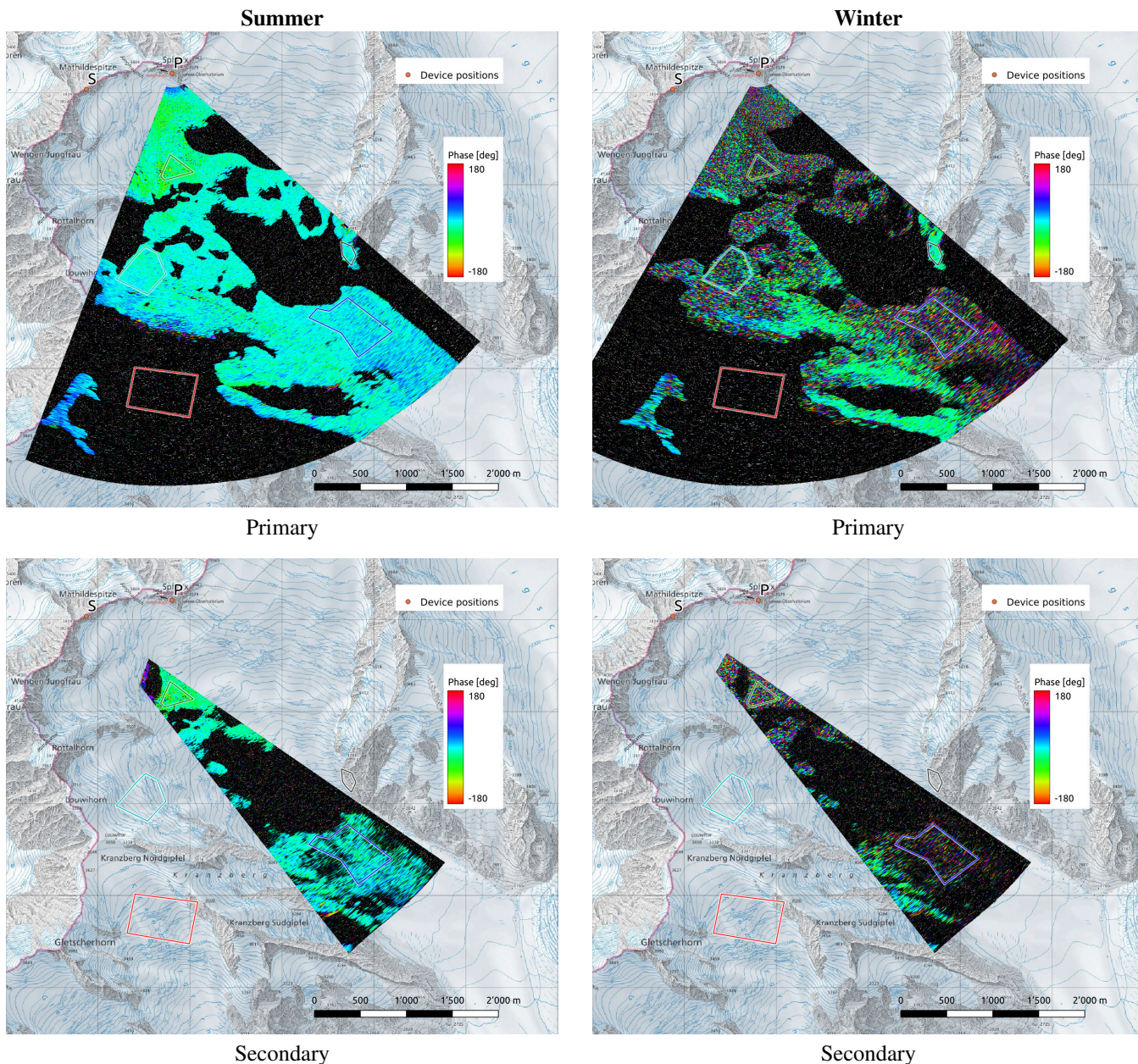


Fig. 14. Comparison of the observed CPD for the summer (left) and winter (right) seasons, for the primary (top, monostatic) and the secondary (bottom, bistatic) dataset. The acquisitions were taken in the evening. In order to enhance the signal, 10 consecutive interferograms were coherently averaged. Compared to the morning acquisitions (Fig. 13), the phase gradient in summer has flattened and the values are closer to zero throughout the scene. In winter, the high rate of spatial variation of CPD remains throughout the day.

the zero value with increasing range. In SnowScat observations of fresh snow at Ku-band [11, Figure 6] (note that the values in the referenced figure show  $\phi_{VV-HH}$ ), the  $\phi_{HH-VV}$  value was observed to be increasingly negative with increasing incidence angle, also a trend opposite to our observations. It should be noted however that the snow and observation conditions in these mentioned publications greatly differed from the setup and conditions of our observations, since our observations in summer were observing aged seasonal snow cover which has repeatedly melted and refrozen over the course of the preceding season. Determination of the precise cause of the observed CPD behaviour remains an open question which

certainly warrants further quantitative analysis.

Temporally, the summer CPD observations show that as liquid water content increases throughout the day, for all ROIs the phase difference shifts towards zero. This is in agreement with the interpretation that liquid water reduces penetration and thus the scattering behavior becomes more surface-like. Afterwards, over night when the snow cover refreezes, the CPD recovers towards its original value. A similar trend was observed in melting and refreezing snow at 95 GHz in [96, Figure 7], where the accumulation of fresh snow cover observed under a 60° incidence angle caused a strong negative value of  $\phi_{HH-VV}$  which quickly reverted towards zero once the

### Bistatic acquisitions, $\phi_{HV-VH}$

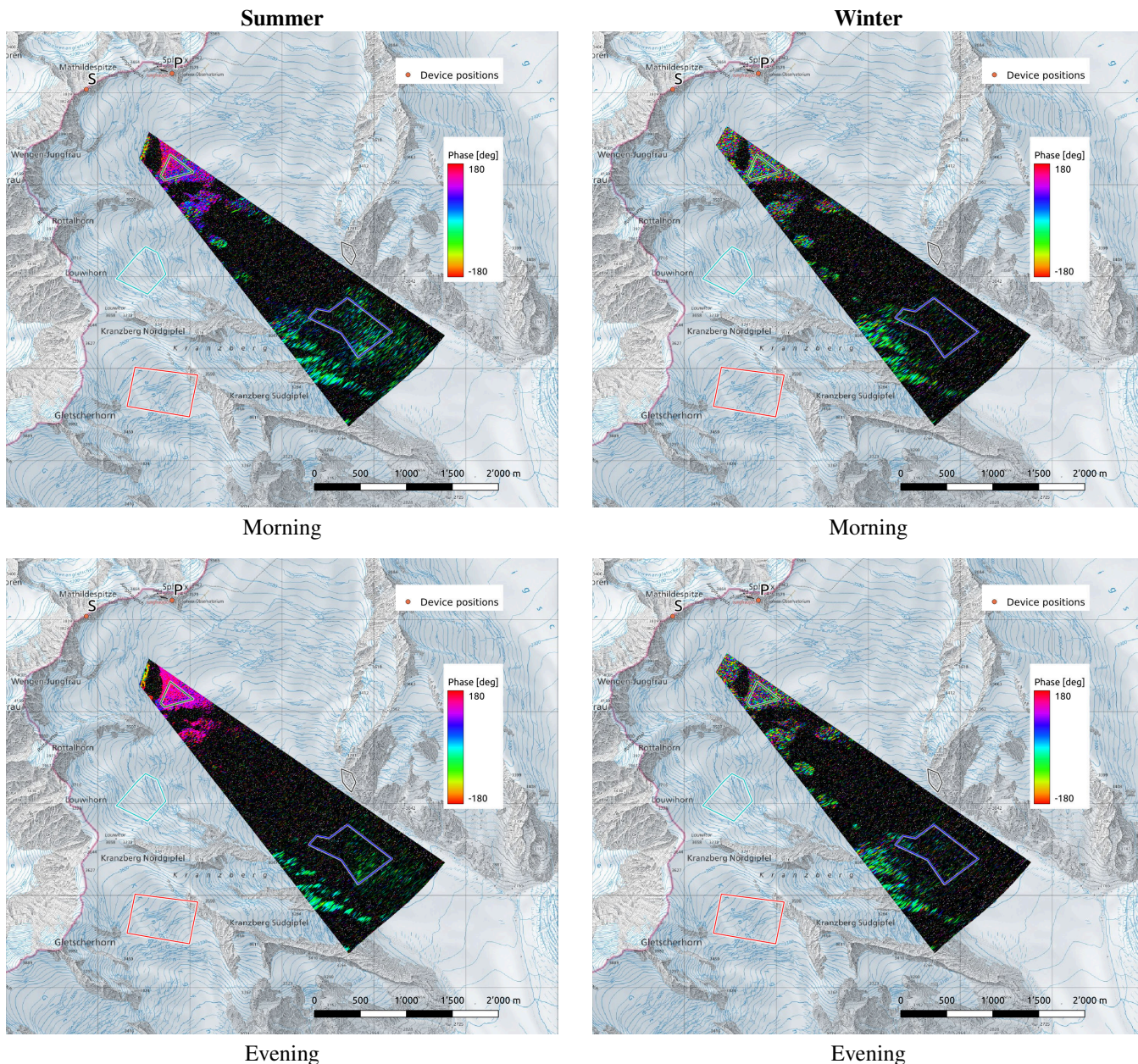


Fig. 15. Comparison of the cross-polar phase difference (XPD) observed by the secondary (bistatic) device, for the summer (left) and winter (right) seasons, for morning (top) and evening (bottom) acquisition time respectively. In order to enhance the signal, 10 consecutive interferograms were coherently averaged. For both seasons, the bistatic acquisitions show significant deviations from this zero value throughout the scene. In summer, in the near range at steeper incidence angles and large bistatic angle the XPD has a large value near  $180^\circ$ . With increasing range and incidence angle (and decreasing bistatic angle), this value appears to reduce towards zero, however precise interpretation is difficult due to low coverage of medium bistatic angles. In the evening, the bistatic XPD in summer has a smoother behaviour, however the strong deviation from the zero value remains. In winter, the XPD exhibits similar behaviour to CPD, varying considerably on short spatial scales. Even with  $10\times$  coherent averaging, the bistatic dataset exhibits very low SNR in the far range.

snow cover started melting.

In winter, a high rate of spatial variation of the CPD is observed, which can be attributed to a high contribution of volume scattering [48], together with a range cell size orders of magnitude larger than the wavelength, causing the positions of the HH and VV phase centers to vary on scales longer than the wavelength. Only the exposed rock face maintains the zero value of CPD, as expected for surface-type scattering. This has implications for scattering models which might aim to invert the CPD for estimates of structural anisotropy or

depth – this approach is often applied at longer wavelengths [11], [13]. However, due to the short Ku-band wavelength, even small values and variations of anisotropy or relatively short depths can cause sufficient phase delay between the two polarizations so as to cause phase-wrapping. We confirmed this by an exploratory analysis of the model presented in [13] which relates the CPD to snow grain shape anisotropy – it has shown that at the Ku-band, with a density fraction value of 0.3 and snow depth of 3m even small variation of any input model parameter causes considerable CPD change and

phase wrapping. This is corroborated by the observed winter data which shows a high rate of spatial variation of CPD even in areas which otherwise appear uniform both visually and in terms of observed backscatter intensity. This variation and phase wrapping makes simple parameter inversion challenging since there is no bijective function between CPD and model parameter values.

However, while the CPD in winter might appear to behave like noise spatially, it remains temporally stable for any particular point on scales of minutes to hours. Thus, by monitoring the CPD with a sufficient temporal resolution, one can monitor this CPD evolution and possibly derive information about the temporal influence of parameters that affect the CPD, such as redistribution and settling of snowpack. This temporal evolution could be particularly interesting to observe just after fresh snowfall – this did unfortunately not occur during our observation windows, but is an observation scenario of interest for future investigations.

2) *Cross-polar phase difference*: The cross-polar phase difference  $\phi_{HV-VH}$  confirms the validity of the reciprocity principle ( $S_{HV} = S_{VH}$ ), as all monostatic datasets (supplementary Fig. S7) exhibit a zero value of  $\phi_{HV-VH}$ , regardless of the scattering medium. However it exhibits a very interesting behaviour in the bistatic datasets (Fig. 15). In winter, it varies considerably on short spatial scales, similarly to the cross-polar phase difference. This can also be interpreted as a large contribution of volume scattering which causes a large variation of the HV and VH phase center positions.

In summer, a large positive value of  $\phi_{HV-VH}$  (approx.  $+150^\circ$ ) is observed in the “Glacier head” ROI. This value appears to further increase with increase of liquid water content due to snowmelt. In the far range (and low bistatic angles), the XPD appears to trend toward the zero value, however the SNR is relatively weak due to the long range, use of low gain antennas, and absorption by liquid water.

One interpretation of the non-zero XPD value can be proposed as a combination of snow birefringence (which also causes the CPD [11]) and a geometric effect caused by the difference between local incidence angles of the transmission and reception legs of the scattered signal (i.e., a different local incidence angle from the point of view of the primary and of the secondary device). This can cause a different phase delay contribution of the two journey segments (the primary-to-scatterer segment and the scatterer-to-secondary segment), which thus do not cancel each other out between the HV and VH channels as they would when monostatic observations are made – Fig. 16 visualizes this interpretation. To the best of our knowledge, there are no similar observations of snow cover at large bistatic angles at radio frequencies available in literature to date, and thus no comparisons with results from other observations can be made. The definitive identification of the mechanism causing the non-zero XPD value remains an open question which certainly invites further investigation.

Regardless of the cause, both the summer and the winter observations show that non-reciprocal backscatter does occur in snow cover at non-zero bistatic angles, and thus care has to be taken not to automatically assume reciprocity during calibration/analysis of bistatic radar backscatter over snow-

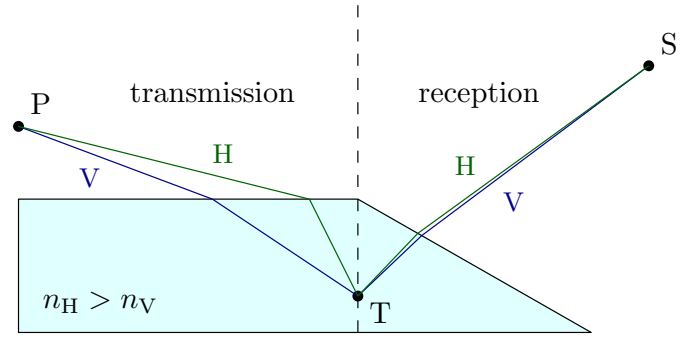


Fig. 16. Possible interpretation of non-zero  $\phi_{HV-VH}$  value caused by combination of birefringence of the snow pack (i.e. difference in refractive indices  $n_H$  and  $n_V$ ) and difference in incidence angles of the transmission and reception legs of the signal's path. The transmission leg causes a significant difference between the phase delays of the H- and V- polarized waves. The reception leg then causes a much smaller difference in the opposite direction, thus the combined VH pathway accumulates a longer phase delay than the HV pathway, resulting in positive value of  $\phi_{HV-VH}$ . In the monostatic case (where both transmission and reception paths occur on the left side of this diagram), the phase differential accumulated during the transmission leg is cancelled out by the reversed differential during the reception leg.

covered regions.

## V. CONCLUSION

In this publication we presented the first application of a long-baseline bistatic KAPRI radar setup to monitoring of natural environments. To the best of our knowledge, this dataset, acquired on top of the Jungfraufirn region of the Great Aletsch Glacier, provides the first polarimetric characterization of Ku-band backscatter from snow-covered areas at non-negligible bistatic angles on range scales of kilometers. The observations revealed high variability of polarimetric properties of backscatter from the observed snow cover between the late summer and late winter seasons, and in some cases also variability between the monostatic and bistatic backscatter, as well as temporal variability in summer.

We observed that temporal decorrelation of snow cover in the observed area at Ku-band occurs on timescales of hours, with coherence reducing to  $1/e$  within time ranging between 4 and 12 hours. While this value might be different in other times of year and areas, the timescale of hours provides an order-of-magnitude estimate of the upper limit on the revisit time of repeat-pass methods such as differential interferometry or SAR tomography. The limit on the scale of hours (or lower tens of hours) will make using these methods with spaceborne Ku-band systems extremely challenging, since spaceborne systems usually have revisit times on the order of days.

The second-order polarimetric parameters, the entropy  $H$  and mean alpha angle  $\bar{\alpha}$  exhibit an expected trend of a lower value in summer when the snow cover has aged and liquid water content causes dominance of surface scattering, and a higher value in winter when fresh snow allows deep penetration and occurrence of a higher diversity of scattering processes.

The polarization phase differences  $\phi_{HH-VV}$  and  $\phi_{HV-VH}$  show a very interesting behavior, both between the two seasons, and between monostatic and bistatic acquisitions. The CPD in winter varies considerably on short spatial

scales, which confirms that CPD-based inversion methods are challenging to apply at Ku-band due to the phase-wrapping tendency when observing snow layers thicker than several tens of centimeters. In summer, it exhibits a smooth incidence-angle-dependent trend, and its value also exhibits an intra-day cycle, which can likely be attributed to changes in liquid water content of the snow cover. The cross-polar phase difference exhibits an expected zero value in all monostatic datasets (as seen in supplementary Fig. S7), however in the bistatic datasets there is a substantial deviation from this zero value. This indicates the presence of non-reciprocal scattering behaviours at non-zero bistatic angles in snow, which has implications both for snow modeling using bistatic data, as well as polarimetric calibration procedures which can no longer rely on the reciprocity principle.

Besides the above-mentioned information about behaviour of polarimetric parameters at Ku-band, lessons learned from the two observation campaigns also suggest attractive future observation targets, such as the observation of the minute-scale temporal behaviour of polarization phase differences during and immediately after fresh snowfall, as well as long-term monitoring of the transition from fresh winter snow to refrozen summer snow. The presented data can also already serve as a reference overview for polarimetric Ku-band scattering behaviour of snow under a variety of conditions, which can aid planning and development of airborne and spaceborne missions operating at similar wavelengths.

#### ACKNOWLEDGMENTS

We acknowledge that the International Foundation High Altitude Research Stations Jungfraujoch and Gornergrat (HF-SJG), 3012 Bern, Switzerland, made it possible for us to carry out our experiments at the High Altitude Research Station at Jungfraujoch. We thank the custodians Daniela Bissig, Erich Furrer, and Christine and Ruedi Käser for the support of our activities.

We would also like to thank Michael Arnold, Jorit Schmelzle, and Pol Villalvilla for their invaluable support during campaigns, and Silvan Leinss and Charles Werner for their technical support regarding radar operation. Furthermore, we would like to thank Marc Rodriguez-Cassola, Keith Morrison, Jordi Mallorqui, and 4 anonymous reviewers for their feedback on the manuscript.

Map underlay: Landeskarte 1:25000, © Federal Office of Topography swisstopo.

#### REFERENCES

[1] A. W. Nolin, "Recent advances in remote sensing of seasonal snow," *Journal of Glaciology*, vol. 56, no. 200, pp. 1141–1150, 2010.

[2] J. King, R. Kelly, A. Kasurak, C. Duguay, G. Gunn, N. Rutter, T. Watts, and C. Derksen, "Spatio-temporal influence of tundra snow properties on Ku-band (17.2 GHz) backscatter," *Journal of Glaciology*, vol. 61, no. 226, pp. 267–279, 2015.

[3] J. Lemmetyinen, A. Kontu, J. Pulliainen, J. Vehviläinen, K. Rautiainen, A. Wiesmann, C. Mätzler, C. Werner, H. Rott, T. Nagler, M. Schneebeli, M. Proksch, D. Schüttemeyer, M. Kern, and M. W. J. Davidson, "Nordic Snow Radar Experiment," *Geoscientific Instrumentation, Methods and Data Systems*, vol. 5, no. 2, pp. 403–415, 2016.

[4] L. Tsang, M. Durand, C. Derksen, A. P. Barros, D.-H. Kang, H. Lievens, H.-P. Marshall, J. Zhu, J. Johnson, J. King, J. Lemmetyinen, M. Sandells, N. Rutter, P. Siqueira, A. Nolin, B. Osmanoglu, C. Vuyovich, E. J. Kim, D. Taylor, I. Merkouriadi, L. Brucker, M. Navari, M. Dumont, R. Kelly, R. S. Kim, T.-H. Liao, and X. Xu, "Review Article: Global Monitoring of Snow Water Equivalent using High Frequency Radar Remote Sensing," *The Cryosphere Discussions*, vol. 2021, pp. 1–57, 2021. [Online]. Available: <https://tc.copernicus.org/preprints/tc-2021-295/>

[5] A. Thompson, R. Kelly, and J. King, "Sensitivity of Ku- and X-Band Radar Observations to Seasonal Snow in Ontario, Canada," *Canadian Journal of Remote Sensing*, vol. 45, no. 6, pp. 829–846, 2019. [Online]. Available: <https://doi.org/10.1080/07038992.2019.1704621>

[6] J. Shi and J. Dozier, "Mapping seasonal snow with SIR-C/X-SAR in mountainous areas," *Remote Sensing of Environment*, vol. 59, no. 2, pp. 294–307, 1997. [Online]. Available: <https://www.sciencedirect.com/science/article/pii/S0034425796001460>

[7] N. Rutter, M. J. Sandells, C. Derksen, J. King, P. Toose, L. Wake, T. Watts, R. Essery, A. Roy, A. Royer, P. Marsh, C. Larsen, and M. Sturm, "Effect of snow microstructure variability on Ku-band radar snow water equivalent retrievals," *The Cryosphere*, vol. 13, no. 11, pp. 3045–3059, 2019. [Online]. Available: <https://tc.copernicus.org/articles/13/3045/2019/>

[8] C. Derksen, J. Lemmetyinen, J. King, S. Belair, C. Garnaud, M. Lapointe, Y. Crevier, G. Burbidge, and P. Siqueira, "A Dual-Frequency Ku-Band Radar Mission Concept for Seasonal Snow," in *IGARSS 2019 - 2019 IEEE International Geoscience and Remote Sensing Symposium*, 2019, pp. 5742–5744.

[9] A. Wiesmann, C. Mätzler, and T. Weise, "Radiometric and structural measurements of snow samples," *Radio Science*, vol. 33, no. 2, pp. 273–289, mar 1998. [Online]. Available: <http://dx.doi.org/10.1029/97RS02746><http://doi.wiley.com/10.1029/97RS02746>

[10] J. Lemmetyinen, C. Derksen, P. Toose, M. Proksch, J. Pulliainen, A. Kontu, K. Rautiainen, J. Seppänen, and M. Hallikainen, "Simulating seasonally and spatially varying snow cover brightness temperature using HUT snow emission model and retrieval of a microwave effective grain size," *Remote Sensing of Environment*, vol. 156, pp. 71–95, 2015. [Online]. Available: <http://dx.doi.org/10.1016/j.rse.2014.09.016><https://www.sciencedirect.com/science/article/pii/S0034425714003605>

[11] S. Leinss, H. Löwe, M. Proksch, J. Lemmetyinen, A. Wiesmann, and I. Hajnsek, "Anisotropy of seasonal snow measured by polarimetric phase differences in radar time series," *Cryosphere*, vol. 10, no. 4, pp. 1771–1797, 2016.

[12] N. M. Rathmann, D. A. Lilien, A. Grinsted, T. A. Gerber, T. J. Young, and D. Dahl-Jensen, "On the limitations of using polarimetric radar sounding to infer the crystal orientation fabric of ice masses," *Geophysical Research Letters*, 2021.

[13] G. Parrella, I. Hajnsek, and K. P. Papathanassiou, "Retrieval of Firn Thickness by Means of Polarisation Phase Differences in L-Band SAR Data," *Remote Sensing*, vol. 13, no. 21, 2021. [Online]. Available: <https://www.mdpi.com/2072-4292/13/21/4448>

[14] H. Rott, D. W. Cline, C. Duguay, R. Essery, P. Etchevers, I. Hajnsek, M. Kern, G. Macelloni, E. Malnes, J. Pulliainen, and Others, "CoReH2O, a dual frequency radar mission for snow and ice observations," in *2012 IEEE International Geoscience and Remote Sensing Symposium*. IEEE, 2012, pp. 5550–5553.

[15] National Research Council, *Earth Science and Applications from Space: National Imperatives for the Next Decade and Beyond*. Washington, DC: The National Academies Press, 2007. [Online]. Available: <https://nap.nationalacademies.org/catalog/11820/earth-science-and-applications-from-space-national-imperatives-for-the>

[16] C. Derksen, J. King, S. Belair, C. Garnaud, V. Vionnet, V. Fortin, J. Lemmetyinen, Y. Crevier, P. Plourde, B. Lawrence, H. van Mierlo, G. Burbidge, and P. Siqueira, "Development of the Terrestrial Snow Mass Mission," in *2021 IEEE International Geoscience and Remote Sensing Symposium IGARSS*, 2021, pp. 614–617.

[17] J.-S. Lee and E. Pottier, *Polarimetric radar imaging: from basics to applications*. CRC press, 2009.

[18] A.-L. Germond, E. Pottier, and J. Saillard, "Foundations of bistatic radar polarimetry theory," in *Radar 97 (Conf. Publ. No. 449)*, 1997, pp. 833–837.

[19] G. Krieger, A. Moreira, H. Fiedler, I. Hajnsek, M. Werner, M. Younis, and M. Zink, "TanDEM-X: A satellite formation for high-resolution SAR interferometry," *IEEE Transactions on Geoscience and Remote Sensing*, vol. 45, no. 11, pp. 3317–3341, 2007.

[20] P. Rizzoli, M. Martone, H. Rott, and A. Moreira, "Characterization of Snow Facies on the Greenland Ice Sheet Observed by TanDEM-X

- Interferometric SAR Data," *Remote Sensing*, vol. 9, no. 4, 2017. [Online]. Available: <https://www.mdpi.com/2072-4292/9/4/315>
- [21] S. Leinss and P. Bernhard, "TanDEM-X: Deriving InSAR Height Changes and Velocity Dynamics of Great Aletsch Glacier," *IEEE Journal of Selected Topics in Applied Earth Observations and Remote Sensing*, vol. 14, pp. 4798–4815, 2021.
- [22] M. Stefko, S. Leinss, O. Frey, and I. Hajnsek, "Coherent backscatter enhancement in bistatic Ku- and X-band radar observations of dry snow," *Cryosphere*, vol. 16, no. 7, pp. 2859–2879, 2022. [Online]. Available: <https://tc.copernicus.org/articles/16/2859/2022/>
- [23] P. Lopez-Dekker, H. Rott, P. Prats-Iraola, B. Chapron, K. Scipal, and E. D. Witte, "Harmony: an Earth Explorer 10 Mission Candidate to Observe Land, Ice, and Ocean Surface Dynamics," in *IGARSS 2019 - 2019 IEEE International Geoscience and Remote Sensing Symposium*. IEEE, jul 2019, pp. 8381–8384. [Online]. Available: <https://ieeexplore.ieee.org/document/8897983/>
- [24] A. Moccia, G. Rufino, M. D'Errico, G. Alberti, and G. Salzillo, "BISAT: A bistatic SAR for earth observation," in *International Geoscience and Remote Sensing Symposium (IGARSS)*, vol. 5. IEEE, 2002, pp. 2628–2630. [Online]. Available: <http://ieeexplore.ieee.org/document/1026723/>
- [25] D. Massonnet, "The interferometric cartwheel: A constellation of passive satellites to produce radar images to be coherently combined," *International Journal of Remote Sensing*, vol. 22, no. 12, pp. 2413–2430, jan 2001. [Online]. Available: <https://www.tandfonline.com/doi/full/10.1080/01431160118952>
- [26] H. A. Zebker, T. G. Farr, R. P. Salazar, and T. H. Dixon, "Mapping the World's Topography Using Radar Interferometry: The TOPSAT Mission," *Proceedings of the IEEE*, vol. 82, no. 12, pp. 1774–1786, 1994. [Online]. Available: <http://ieeexplore.ieee.org/document/338070/>
- [27] N. Gebert, B. Carnicero Dominguez, M. W. J. Davidson, M. Diaz Martin, and P. Silvestrin, "SAOCOM-CS - A passive companion to SAOCOM for single-pass L-band SAR interferometry," in *EUSAR 2014; 10th European Conference on Synthetic Aperture Radar*, 2014, pp. 1–4.
- [28] S. Tan, W. Chang, L. Tsang, J. Lemmetyinen, and M. Proksch, "Modeling Both Active and Passive Microwave Remote Sensing of Snow Using Dense Media Radiative Transfer (DMRT) Theory with Multiple Scattering and Backscattering Enhancement," *IEEE Journal of Selected Topics in Applied Earth Observations and Remote Sensing*, vol. 8, no. 9, pp. 4418–4430, 2015.
- [29] A. Wiesmann and C. Mätzler, "Microwave emission model of layered snowpacks," *Remote sensing of environment*, vol. 70, no. 3, pp. 307–316, 1999.
- [30] A. Rees, J. Lemmetyinen, C. Derksen, J. Pulliainen, and M. English, "Observed and modelled effects of ice lens formation on passive microwave brightness temperatures over snow covered tundra," *Remote Sensing of Environment*, vol. 114, no. 1, pp. 116–126, 2010.
- [31] G. Parrella, I. Hajnsek, and K. P. Papathanassiou, "Model-Based Interpretation of PolSAR Data for the Characterization of Glacier Zones in Greenland," *IEEE Journal of Selected Topics in Applied Earth Observations and Remote Sensing*, vol. 14, pp. 11593–11607, 2021.
- [32] A. Wiesmann, C. Werner, T. Strozzi, C. Mätzler, T. Nagler, H. Rott, M. Schneebeli, and U. Wegmüller, "SnowScat, X-to Ku-band scatterometer development," in *ESA Living Planet Symposium*, vol. 686, 2010, p. 160.
- [33] J. Dozier and J. Shi, "Estimation of snow water equivalence using sir-c/x-sar. i. inferring snow density and subsurface properties," *IEEE Transactions on Geoscience and Remote Sensing*, vol. 38, pp. 2465–2474, 2000. [Online]. Available: <http://ieeexplore.ieee.org/document/885195/>
- [34] A. Patil, G. Singh, C. Rudiger, S. Mohanty, S. Kumar, and Snehamani, "A novel approach for the snow water equivalent retrieval using x-band polarimetric synthetic aperture radar data," *IEEE Transactions on Geoscience and Remote Sensing*, vol. 59, pp. 3753–3763, 5 2021.
- [35] S. Manickam, A. Bhattacharya, G. Singh, and Y. Yamaguchi, "Estimation of snow surface dielectric constant from polarimetric sar data," *IEEE Journal of Selected Topics in Applied Earth Observations and Remote Sensing*, vol. 10, pp. 211–218, 1 2017.
- [36] M. Surendar, A. Bhattacharya, G. Singh, and G. Venkataraman, "Estimation of snow density using full-polarimetric synthetic aperture radar (sar) data," *Physics and Chemistry of the Earth*, vol. 83-84, pp. 156–165, 2015.
- [37] X. Xu, L. Tsang, and S. Yueh, "Electromagnetic Models of Co/Cross Polarization of Bicontinuous/DMRT in Radar Remote Sensing of Terrestrial Snow at X- and Ku-band for CoReH2O and SCLP Applications," *IEEE Journal of Selected Topics in Applied Earth Observations and Remote Sensing*, vol. 5, no. 3, pp. 1024–1032, jun 2012. [Online]. Available: <http://doi.wiley.com/10.1029/97RS02746https://ieeexplore.ieee.org/document/6185696/>
- [38] W. Chang, K. H. Ding, L. Tsang, and X. Xu, "Microwave Scattering and Medium Characterization for Terrestrial Snow with QCA-Mie and Bicontinuous Models: Comparison Studies," *IEEE Transactions on Geoscience and Remote Sensing*, vol. 54, no. 6, pp. 3637–3648, 2016.
- [39] A. Muhuri, S. Manickam, A. Bhattacharya, and Snehamani, "Snow cover mapping using polarization fraction variation with temporal radarsat-2 c-band full-polarimetric sar data over the indian himalayas," *IEEE Journal of Selected Topics in Applied Earth Observations and Remote Sensing*, vol. 11, pp. 2192–2209, 7 2018.
- [40] T. Jagdhuber, J. Stockamp, I. Hajnsek, and R. Ludwig, "Identification of soil freezing and thawing states using sar polarimetry at c-band," *Remote Sensing*, vol. 6, pp. 2008–2023, 2014.
- [41] A. Muhuri, S. Manickam, and A. Bhattacharya, "Scattering mechanism based snow cover mapping using radarsat-2 c-band polarimetric sar data," *IEEE Journal of Selected Topics in Applied Earth Observations and Remote Sensing*, vol. 10, pp. 3213–3224, 7 2017.
- [42] Y. L. S. Tsai, A. Dietz, N. Oppelt, and C. Kuenzer, "Remote sensing of snow cover using spaceborne SAR: A review," *Remote Sensing*, vol. 11, no. 12, 2019.
- [43] Snehamani, M. K. Singh, R. D. Gupta, A. Bhardwaj, and P. K. Joshi, "Remote sensing of mountain snow using active microwave sensors: a review," *Geocarto International*, vol. 30, no. 1, pp. 1–27, 2015. [Online]. Available: <https://doi.org/10.1080/10106049.2014.883434>
- [44] S. Awasthi and D. Varade, "Recent advances in the remote sensing of alpine snow: a review," *GIScience & Remote Sensing*, vol. 58, no. 6, pp. 852–888, 2021. [Online]. Available: <https://doi.org/10.1080/15481603.2021.1946938>
- [45] A. J. Dietz, C. Kuenzer, U. Gessner, and S. Dech, "Remote sensing of snow – a review of available methods," *International Journal of Remote Sensing*, vol. 33, no. 13, pp. 4094–4134, 2012. [Online]. Available: <https://doi.org/10.1080/01431161.2011.640964>
- [46] C. Mätzler, "Applications of the interaction of microwaves with the natural snow cover," *Remote Sensing Reviews*, vol. 2, no. 2, pp. 259–387, 1987. [Online]. Available: <https://doi.org/10.1080/02757258709532086>
- [47] O. Frey, C. L. Werner, R. Caduff, and A. Wiesmann, "Tomographic Profiling with Snowscat Within the ESA Snowlab Campaign: Time Series of Snow Profiles Over three Snow Seasons," in *IGARSS 2018 - 2018 IEEE International Geoscience and Remote Sensing Symposium*. IEEE, jul 2018, pp. 6512–6515. [Online]. Available: <https://ieeexplore.ieee.org/document/8517692/>
- [48] S. Leinss, G. Parrella, and I. Hajnsek, "Snow height determination by polarimetric phase differences in X-Band SAR Data," *IEEE Journal of Selected Topics in Applied Earth Observations and Remote Sensing*, vol. 7, no. 9, pp. 3794–3810, 2014.
- [49] A. G. Fore, B. D. Chapman, B. P. Hawkins, S. Hensley, C. E. Jones, T. R. Michel, and R. J. Muellerschoen, "UAVSAR polarimetric calibration," *IEEE Transactions on Geoscience and Remote Sensing*, vol. 53, no. 6, pp. 3481–3491, 2015.
- [50] K. Sarabandi, F. T. Ulaby, and M. A. Tassoudji, "Calibration of Polarimetric Radar Systems With Good Polarization Isolation," *IEEE Transactions on Geoscience and Remote Sensing*, vol. 28, no. 1, pp. 70–75, 1990.
- [51] P. López-Dekker, H. Rott, P. Prats-Iraola, B. Chapron, K. Scipal, and E. D. Witte, "Harmony: an earth explorer 10 mission candidate to observe land, ice, and ocean surface dynamics," in *IGARSS 2019 - 2019 IEEE International Geoscience and Remote Sensing Symposium*, 2019, pp. 8381–8384.
- [52] F. Ulaby, K. Sarabandi, and A. Nashashibi, "Statistical properties of the mueller matrix of distributed targets," *IEE Proceedings F Radar and Signal Processing*, vol. 139, p. 136, 1992. [Online]. Available: <https://digital-library.theiet.org/content/journals/10.1049/ip-f-2.1992.0017>
- [53] M. Migliaccio, F. Nunziata, and A. Gambardella, "On the co-polarized phase difference for oil spill observation," *International Journal of Remote Sensing*, vol. 30, pp. 1587–1602, 3 2009.
- [54] A. Reigber, K. Papathanassiou, M. Jger, and R. Scheiber, "First results of multispectral polarimetry and single-pass polinsar with the f-sar airborne sar instrument," in *2013 IEEE International Geoscience and Remote Sensing Symposium - IGARSS*, 2013, pp. 2305–2308.
- [55] E. Everaere, "Polarimetry in bistatic configuration for ultra high frequency radar measurements on forest environment," Ph.D. dissertation, Ecole Polytechnique, 2015.

- [56] S. Cloude, *Polarisation: Applications in Remote Sensing*. Oxford University Press, oct 2009. [Online]. Available: <https://academic.oup.com/book/11554>
- [57] R. Touzi, "Target Scattering Decomposition in Terms of Roll-Invariant Target Parameters," *IEEE Transactions on Geoscience and Remote Sensing*, vol. 45, no. 1, pp. 73–84, jan 2007. [Online]. Available: <http://ieeexplore.ieee.org/document/4039635/>
- [58] L. Bombrun, "Roll-invariant target decomposition in bistatic polarimetric sar imagery," *Canadian Journal of Remote Sensing*, vol. 37, pp. 204–212, 1 2011.
- [59] S. E. Park, "Variations of microwave scattering properties by seasonal freeze/thaw transition in the permafrost active layer observed by alos pulsar polarimetric data," *Remote Sensing*, vol. 7, pp. 17 135–17 148, 12 2015.
- [60] D. Varade, G. Singh, O. Dikshit, and S. Manickam, "Identification of snow using fully polarimetric sar data based on entropy and anisotropy," *Water Resources Research*, vol. 56, 2 2020.
- [61] D. Varade, S. Manickam, O. Dikshit, G. Singh, and Snehmani, "Modelling of early winter snow density using fully polarimetric c-band sar data in the indian himalayas," *Remote Sensing of Environment*, vol. 240, 4 2020.
- [62] S. Leinss, A. Wiesmann, J. Lemmetyinen, and I. Hajnsek, "Snow Water Equivalent of Dry Snow Measured by Differential Interferometry," *IEEE Journal of Selected Topics in Applied Earth Observations and Remote Sensing*, vol. 8, no. 8, pp. 3773–3790, 2015.
- [63] H. A. Zebker, J. Villaseñor, and Others, "Decorrelation in interferometric radar echoes," *IEEE Transactions on geoscience and remote sensing*, vol. 30, no. 5, pp. 950–959, 1992.
- [64] R. L. Hawley, E. M. Morris, R. Cullen, U. Nixdorf, A. P. Shepherd, and D. J. Wingham, "ASIRAS airborne radar resolves internal annual layers in the dry-snow zone of Greenland," *Geophysical Research Letters*, vol. 33, no. 4, 2006. [Online]. Available: <https://agupubs.onlinelibrary.wiley.com/doi/abs/10.1029/2005GL025147>
- [65] S. Yueh, D. Cline, and K. Elder, "Airborne Ku-band radar remote sensing of terrestrial snow cover," *International Geoscience and Remote Sensing Symposium (IGARSS)*, vol. 47, no. 10, pp. 1211–1214, 2007.
- [66] A. Coccia, C. Trampuz, M. Ortolani, R. Turtolo, T. Wiewering, and A. Meta, "Deployment of the SnowSAR sensor in the SnowEx campaign by NASA and preliminary results," in *2017 IEEE International Geoscience and Remote Sensing Symposium (IGARSS)*, 2017, pp. 1403–1405.
- [67] H. M.-J. Cantalloube, "Imaging of Snow/Ice Subsurface Features from Airborne Sar At UHF, L And X Band. The Onera Sar Campaign in South Greenland," in *IGARSS 2019 - 2019 IEEE International Geoscience and Remote Sensing Symposium*, 2019, pp. 4157–4160.
- [68] B. Osmanoglu, R. Rincon, Q. Bonds, P. Racette, L. Brucker, and M. Perrine, "SWESARR: Snow Water Equivalent Radar and Radiometer," in *AGU Fall Meeting Abstracts*, vol. 2018, 2018, pp. C13D–1173.
- [69] J. Lemmetyinen, J. Cohen, A. Kontu, J. Vehviläinen, H.-R. Hannula, I. Merkouriadi, S. Scheiblauer, H. Rott, T. Nagler, E. Ripper, K. Elder, H.-P. Marshall, R. Fromm, M. Adams, C. Derksen, J. King, A. Meta, A. Coccia, N. Rutter, M. Sandells, G. Macelloni, E. Santi, M. Leduc-Leballeur, R. Essery, C. Menard, and M. Kern, "Airborne SnowSAR data at X- and Ku- bands over boreal forest, alpine and tundra snow cover," *Earth System Science Data Discussions*, vol. 2021, pp. 1–49, 2021. [Online]. Available: <https://essd.copernicus.org/preprints/essd-2021-239/>
- [70] J. M. L. King, R. Kelly, A. Kasurak, C. Duguay, G. Gunn, and J. B. Mead, "UW-Scat: A Ground-Based Dual-Frequency Scatterometer for Observation of Snow Properties," *IEEE Geoscience and Remote Sensing Letters*, vol. 10, no. 3, pp. 528–532, 2013.
- [71] X. Xu, C. A. Baldi, J.-W. De Bleser, Y. Lei, S. Yueh, and D. Esteban-Fernandez, "Multi-Frequency Tomography Radar Observations of Snow Stratigraphy at Fraser During SnowEx," in *IGARSS 2018 - 2018 IEEE International Geoscience and Remote Sensing Symposium*, 2018, pp. 6269–6272.
- [72] X. Xu, H. Shen, H. Xu, and L. Tsang, "Modeling Multi-Frequency Tomograms for Snow Stratigraphy," in *IGARSS 2020 - 2020 IEEE International Geoscience and Remote Sensing Symposium*, 2020, pp. 3436–3439.
- [73] Y. Lei, X. Xu, C. A. Baldi, J.-W. De Bleser, S. H. Yueh, D. Esteban-Fernandez, K. Elder, B. Starr, and P. Siqueira, "Dry Snow Parameter Retrieval With Ground-Based Single-Pass Synthetic Aperture Radar Interferometry," *IEEE Transactions on Geoscience and Remote Sensing*, vol. 60, pp. 1–14, 2022.
- [74] O. Frey, C. L. Werner, R. Caduff, and A. Wiesmann, "A time series of tomographic profiles of a snow pack measured with SnowScat at X-/Ku-band," in *2016 IEEE International Geoscience and Remote Sensing Symposium (IGARSS)*. IEEE, jul 2016, pp. 17–20. [Online]. Available: <http://ieeexplore.ieee.org/document/7728995/>
- [75] —, "Inversion of SNOW structure parameters from time series of tomographic measurements with SnowScat," in *2017 IEEE International Geoscience and Remote Sensing Symposium (IGARSS)*. IEEE, jul 2017, pp. 2472–2475. [Online]. Available: <http://ieeexplore.ieee.org/document/8127494/>
- [76] C. Werner, O. Frey, R. Naderpour, A. Wiesmann, M. Suess, and U. Wegmüller, "Aperture Synthesis and Calibration of the WBSCAT Ground-Based Scatterometer," in *2021 IEEE International Geoscience and Remote Sensing Symposium IGARSS*, 2021, pp. 1947–1949.
- [77] A. Wiesmann, R. Caduff, C. Werner, O. Frey, M. Schneebeli, H. Löwe, M. Jaggi, M. Schwank, R. Naderpour, and T. Fehr, "ESA SnowLab Project: 4 Years Of Wide Band Scatterometer Measurements Of Seasonal Snow," in *IGARSS 2019 - 2019 IEEE International Geoscience and Remote Sensing Symposium*, 2019, pp. 5745–5748.
- [78] M. Stefko, O. Frey, C. Werner, and I. Hajnsek, "Calibration and Operation of a Bistatic Real-Aperture Polarimetric-Interferometric Ku-Band Radar," *IEEE Transactions on Geoscience and Remote Sensing*, vol. 60, pp. 1–19, 2022. [Online]. Available: <https://ieeexplore.ieee.org/document/9580835/>
- [79] C. Werner, A. Wiesmann, T. Strozzi, A. Kos, R. Caduff, and U. Wegmüller, "The GPRI multi-mode differential interferometric radar for ground-based observations," in *EUSAR 2012; 9th European Conference on Synthetic Aperture Radar*, 2012, pp. 304–307.
- [80] R. Caduff, A. Kos, F. Schlunegger, B. W. McARDell, and A. Wiesmann, "Terrestrial radar interferometric measurement of hillslope deformation and atmospheric disturbances in the Illgraben debris-flow catchment, Switzerland," *IEEE Geoscience and Remote Sensing Letters*, vol. 11, no. 2, pp. 434–438, feb 2014. [Online]. Available: <http://ieeexplore.ieee.org/document/6558751/>
- [81] T. Strozzi, C. Werner, A. Wiesmann, and U. Wegmüller, "Topography mapping with a portable real-aperture radar interferometer," *IEEE Geoscience and Remote Sensing Letters*, vol. 9, no. 2, pp. 277–281, 2011.
- [82] A. Wiesmann, R. Caduff, and C. Mätzler, "Terrestrial radar observations of dynamic changes in alpine snow," *IEEE Journal of Selected Topics in Applied Earth Observations and Remote Sensing*, vol. 8, no. 7, pp. 3665–3671, jul 2015. [Online]. Available: <http://ieeexplore.ieee.org/document/7059220/>
- [83] S. Baffelli, O. Frey, and I. Hajnsek, "Geostatistical Analysis and Mitigation of the Atmospheric Phase Screens in Ku-Band Terrestrial Radar Interferometric Observations of an Alpine Glacier," *IEEE Transactions on Geoscience and Remote Sensing*, vol. 58, no. 11, pp. 7533–7556, nov 2020. [Online]. Available: <https://ieeexplore.ieee.org/document/9064718/>
- [84] Y. Izumi, O. Frey, S. Baffelli, I. Hajnsek, and M. Sato, "Efficient Approach for Atmospheric Phase Screen Mitigation in Time Series of Terrestrial Radar Interferometry Data Applied to Measure Glacier Velocity," *IEEE Journal of Selected Topics in Applied Earth Observations and Remote Sensing*, vol. 14, pp. 7734–7750, 2021.
- [85] S. Baffelli, O. Frey, and I. Hajnsek, "Polarimetric Analysis of Natural Terrain Observed With a Ku -Band Terrestrial Radar," *IEEE Journal of Selected Topics in Applied Earth Observations and Remote Sensing*, vol. 12, no. 12, pp. 5268–5288, dec 2019. [Online]. Available: <https://ieeexplore.ieee.org/document/8960552/>
- [86] G. Jouvét and M. Huss, "Future retreat of great aletsch glacier," pp. 869–872, 10 2019.
- [87] M. Huss, A. Bauder, M. Funk, and R. Hock, "Determination of the seasonal mass balance of four alpine glaciers since 1865," *Journal of Geophysical Research: Earth Surface*, vol. 113, 3 2008.
- [88] H. Zebker and E. Weber Hoen, "Penetration depths inferred from interferometric volume decorrelation observed over the Greenland Ice Sheet," *IEEE Transactions on Geoscience and Remote Sensing*, vol. 38, no. 6, pp. 2571–2583, 2000. [Online]. Available: <http://ieeexplore.ieee.org/document/885204/>
- [89] I. McLeod, I. G. Cumming, and M. Seymour, "ENVISAT ASAR data reduction: impact on SAR interferometry," *IEEE Transactions on Geoscience and Remote Sensing*, vol. 36, no. 2, pp. 589–602, mar 1998. [Online]. Available: <http://ieeexplore.ieee.org/document/662741/>
- [90] C. Lucas, S. Leinss, Y. Bühler, A. Marino, and I. Hajnsek, "Multipath interferences in ground-based radar data: A case study," *Remote Sensing*, vol. 9, no. 12, pp. 1–19, 2017.
- [91] D. Just and R. Bamler, "Phase statistics of interferograms with applications to synthetic aperture radar," *Applied Optics*, vol. 33,

- no. 20, p. 4361, jul 1994. [Online]. Available: <https://www.osapublishing.org/abstract.cfm?URI=ao-33-20-4361>
- [92] H. H. Ku and Others, "Notes on the use of propagation of error formulas," *Journal of Research of the National Bureau of Standards*, vol. 70, no. 4, pp. 263–273, 1966.
- [93] S. Baffelli, O. Frey, C. Werner, and I. Hajnsek, "Polarimetric Calibration of the Ku-Band Advanced Polarimetric Radar Interferometer," *IEEE Transactions on Geoscience and Remote Sensing*, vol. 56, no. 4, pp. 2295–2311, 2017.
- [94] I. Hajnsek, K. P. Papathanassiou, and S. R. Cloude, "Removal of additive noise in polarimetric eigenvalue processing," in *IGARSS 2001. Scanning the Present and Resolving the Future. Proceedings. IEEE 2001 International Geoscience and Remote Sensing Symposium (Cat. No. 01CH37217)*, vol. 6, 2001, pp. 2778–2780 vol.6.
- [95] E. J. Rignot, "Backscatter model for the unusual radar properties of the Greenland ice sheet," *Journal of Geophysical Research*, vol. 100, no. E5, pp. 9389–9400, 1995.
- [96] P. Chang, J. Mead, E. Knapp, G. Sadowy, R. Davis, and R. McIntosh, "Polarimetric backscatter from fresh and metamorphic snowcover at millimeter wavelengths," *IEEE Transactions on Antennas and Propagation*, vol. 44, no. 1, pp. 58–73, 1996. [Online]. Available: <http://ieeexplore.ieee.org/document/477529/>
- [97] K. Belinska, G. Fischer, T. Nagler, and I. Hajnsek, "Snow Water Equivalent Estimation Using Differential SAR Interferometry and Co-Polar Phase Differences from Airborne SAR Data," *International Geoscience and Remote Sensing Symposium (IGARSS)*, vol. 2022-July, pp. 4545–4548, 2022.
- [98] R. Millan, J. Mougnot, A. Rabatel, and M. Morlighem, "Ice velocity and thickness of the world's glaciers," *Nature Geoscience*, vol. 15, pp. 124–129, 2 2022.
- [99] J. J. Ruiz, J. Lemmetyinen, A. Kontu, R. Tarvainen, R. Vehmas, J. Pulliainen, and J. Praks, "Investigation of environmental effects on coherence loss in sar interferometry for snow water equivalent retrieval," *IEEE Transactions on Geoscience and Remote Sensing*, vol. 60, pp. 1–15, 2022.
- [100] G. Parrella, I. Hajnsek, and K. P. Papathanassiou, "Polarimetric decomposition of L-Band PolSAR backscattering over the austfonna ice cap," *IEEE Transactions on Geoscience and Remote Sensing*, vol. 54, no. 3, pp. 1267–1281, 2016.